

Nanostructures Created by Lasers

E. G. Gamaly, A. V. Rode

Australian National University, Canberra, Australia

CONTENTS

1. Introduction
2. Cluster Formation by Laser Ablation:
Experimental Installations
and Diagnostic Methods
3. Hot Vapor (Plasma) Produced
by Laser Ablation
4. Formation of Nanoclusters
in a Vacuum
5. Nanoclusters Produced Through
the Interaction of Ablated Vapor
with Noble Gas
6. Cluster-Assembled Materials
7. Perspectives on Laser Ablation
for Controllable Production
of Nanoclusters
- Glossary
- References

1. INTRODUCTION

Tiny edifices with a size of around 1–10 nm (1 nm = 10^{-9} m) are called nanocrystals or nanoclusters. These structures are aggregates of atoms or molecules containing from a few atoms to a few thousands atoms. The novelty of these systems relates to the fact that they have an atomic arrangement and material properties drastically different from the same material in bulk. Nanoscience aims at the study of electronic, material, optical, and structural properties of tiny clusters and their composites. The goal of nanotechnology is the production of new and different things—smaller and with new properties. It is emerging as the next technological revolution, promising great advances in many fields, from information technology and medicine to artificial intelligence and environmental restoration.

Richard Feynman in his prophetic lecture “Plenty of Room at the Bottom” in 1959 expressed a strong belief that someday we would be able to manipulate matter on the atomic scale: “The principles of physics, as far as I can see,

do not speak against the possibility of manoeuvring things atom by atom. It is not an attempt to violate any laws; it is something, in principle, that can be done” Thus, the core idea and the ultimate goal of nanotechnology is a realization of “the possibility of manoeuvring things atom by atom”: constructing a new nanomaterial by placing atom by atom at the proper construction site at a proper time. We are still far from realization of this idea in practice; however, many important steps in this direction have been made.

The major problem in nanotechnology lies in the development of efficient methods for the formation of nanoclusters with predictable and controlled size and properties that can then be scaled to industrial production. The primary goal in any method for nanocluster formation is to decompose the initial material into a preferably atomic state via evaporation or ablation and form a beam (or cloud) of hot atoms. The interaction of this beam with the flow of another gas (a noble gas or a reactive one) in a proper temperature-controlled environment creates the temperature and density conditions for the formation of a new structure. The hot atoms from the beam collide with the ambient gas atoms, cool down, and attach to each other, binding and forming a new structure in a self-assembly mode. The newly created material should then be annealed appropriately in order to transform it into a phase state which is stable at room temperature and atmospheric pressure.

The formation of different structures in a self-assembly fashion occurs in a variety of natural systems. In the methods for nanocluster formation, self-assembly is achieved by the proper choice of reacting materials so that they naturally bond with each other in the desired configuration. In theory, one can prepare an atomic mixture in an experimental chamber under carefully controlled conditions and allow the components to assemble themselves. This is the so-called bottom-up approach, or atom-to-atom attachment. In reality the processes of atomic beam formation, cluster creation, and annealing are fast and transient. These processes are very difficult to control and register *in-situ* even with modern diagnostic methods.

A variety of methods have already been proposed and employed for the production of nanoclusters in the past 2 decades, including the use of supersonic nozzle sources, ion beam implantation, methods of colloid chemistry, chemical vapor deposition (CVD), arc discharge, ion sputtering,

laser ablation, and others [1–3]. Methods for the creation of supersonic molecular and atomic beams have allowed one the production of clusters in the gas phase from different materials, including the most refractory and complex systems (fullerenes, carbon and boron nitride nanotubes, metallic and covalent clusters, complex clusters). Nanofilms of different materials and thin layers of matrix-embedded cluster composites have also been successfully deposited and characterized [1–3].

In fact, all methods for nanocluster formation stem from the original experiment for the preparation of so-called “blacks,” the historical predecessor of nanocrystal networks, conceived and implemented by the American physicist Pfund in 1930 [4, 5]. He evaporated bismuth in an imperfect vacuum. The low-density gas fill acts as a confinement and a heat sink for evaporated the atoms. The hot atoms from the evaporation source cool down through collisions with the gas fill and then form tiny droplets when the supersaturated state is achieved. The process comprises three stages: nucleation, growth, and cluster network formation on a substrate [5]. The differences between all of the modern methods for nanocluster formation relate mainly to how the atomic beam is prepared. In this chapter we describe the laser ablation method for the formation and control of an atomic plume which is then used for the formation of various nanostructures under different experimental conditions.

The laser ablation process has a number of remarkable features. First, laser ablation has the highest instantaneous ablation and deposition rate among all known deposition methods, such as electron-beam deposition, magnetron sputtering, and chemical vapor deposition. Second, a laser beam is a “clean” tool: it provides direct energy transfer into the ablated material, and thus there is no source of contamination in the process. Consequently, the laser deposition process maintains the same stoichiometry in the deposited film or in a nanocluster as that in the ablated target. Third, the laser ablation process can operate over a wide range of gas pressures. Finally, it is possible to manipulate the atomic beam created by a short laser pulse at a time scale of picoseconds and a space scale of micrometers.

During the past decade, a number of complicated structures have been successfully produced by laser ablation and deposition. Examples include high-temperature superconducting films [6], various types of nitrides [7–9], complex multicomponent oxides [10, 11], nanocrystalline quantum dots [12], ferroelectric thin films [13], planar lasers, and nonlinear waveguides [14, 15]. Throughout these studies lasers of various wavelengths (from 193 nm to 10.6 μm), pulse durations (from tens of picoseconds to hundreds of nanoseconds), and intensities have been used.

Laser vaporization has been used for the production of nanocluster production since the early seventies, when commercial lasers became available [1, 2, 6]. Metal clusters [16–18], fullerenes [19], carbon and boron nitride nanotubes [20–22], silicon clusters, and many other structures have been produced with laser ablation. In all these studies, commercially available lasers were used as a heating source rather than exploring all the opportunities that a laser offers for controlling beam composition and properties. Extensive studies of laser–matter interaction, including

ablation and the properties of a laser-created plume, were performed within laser fusion projects in major laser laboratories around the world starting in the early sixties [23–26]. Recently it has been understood that many results obtained in laser fusion programs can be usefully employed in laser-assisted methods for nanocluster formation in materials science research.

Laser-assisted nanostructure formation is conventionally performed in a special chamber in which an intense laser beam is focused onto a target from which the desired nanostructure should be formed. Initially, commercial Nd:YAG (neodymium doped yttrium–aluminium garnet) lasers and excimer lasers with pulse durations of 10–30 ns, repetition rates of 10–30 Hz, and average intensities per pulse of $2\text{--}4 \times 10^9 \text{ W/cm}^2$ have been employed for target evaporation [16–18]. Laser evaporation generates a plume with a rather high ion temperature of a few electron volts during the pulse time. However, due to the large time gap between successive pulses, the laser plume cools down below the temperature which is necessary for cluster formation. Therefore, additional heating of the ambient gas was necessary in order to maintain the proper conditions for cluster formation. The target was placed into a furnace with a controlled temperature and with a continuous noble gas flow. With a long (nanoseconds)-pulse, low repetition rate (several Hertz) laser, it is possible to produce a pulsed flow of evaporated vapors with low time-averaged flux intensity.

The use of dual-pulsed Nd:YAG laser vaporization has proved to increase the efficiency of carbon nanotube formation [27]. Furthermore, the use of continuous-wave CO_2 lasers at an intensity level $\sim 10^5 \text{ W/cm}^2$ [28] or an almost continuous 20-ms pulse [29, 30] for evaporation of carbon targets made it possible to obtain a continuous supply of hot carbon atoms into an argon-filled experimental chamber. The collision of hot carbon atoms with cold argon atoms maintains a temperature sufficient for carbon nanotube formation without additional heating in a furnace.

The next step in improving the average vapor beam intensity and control over the density and temperature of the laser-ablated vapor relates to the use of short (a few femtoseconds), intense (average intensity per pulse, $\sim 10^{13}\text{--}10^{14} \text{ W/cm}^2$), low-energy (μJ) pulses delivered at high repetition rates (100 kHz–100 MHz) [31–33]. The high average intensity per pulse allows a significant number of particles, $\sim 10^{11}$ atoms per 100-fs pulse, to be removed during the short pulse time, while the high repetition rate maintains the average atomic beam intensity at a sufficiently high level of 10^{19} atoms/s.

Self-consistent choice of the optimum combination of laser parameters (pulse duration, energy, wavelength, and intensity distribution during the pulse time and in space over the focal spot) along with the target parameters allows one to produce an atomized flow of ablated vapors from any material. The temperature, density, atomic content, and degree of ionization in a cloud of vapors depend on the above combination and therefore can also be controlled.

Ablation with high repetition rate lasers also increases the average temperature of the ablated atomic beam up to 20 times compared with conventional long-pulse low repetition rate lasers. Thus additional heating during cluster formation can be eliminated and the experimental setup

is simplified. The laser beam is continuously scanned over the target surface in order to prevent crater formation and to maintain a constant ablation rate for successive pulses. Fast scanning across a complex target makes possible the coevaporation of different materials. As a result, combinatorial material synthesis in the plume can be implemented. Vapor composition can be varied continuously by adjusting the dwell time on different parts of a composite target.

The laser-ablated atomic beam can be used for the formation of new structures in two fundamentally different experimental situations. In the first operation mode, the ablated plume is used for the deposition of thin films on different substrates in an evacuated chamber. The substrate to be coated is placed in the path of the laser-produced plume; the vapor adheres to the surface to form a nanofilm. In the second operation mode the ablated atomic flow interacts with a different gas fill in a chamber at different pressures, creating nanoclusters and nanocluster networks. The characteristics of the ablated plume are sensitive to a combination of laser and target parameters. Therefore, this combination should be different for the two operation modes mentioned above.

Let us consider thin film deposition by laser ablation. The main drawback to widespread industrial application of lasers for deposition of homogeneous thin films has been the formation of droplets ($0.1\text{--}1\text{ }\mu\text{m}$) in the laser plume, which spoil the surface finish of the deposited film. Many applications require the density of micrometer-sized particles to be less than 1 cm^2 on the surface of the deposited film. The origin of these particles (droplets) relates to inhomogeneities in the target, spatial and time distribution and fluctuations of laser intensity, and the level of absorbed laser energy. While there have been attempts to prevent particles from the target from reaching the substrate using some form of mechanical filtering, there does not appear to have been any satisfactory or universal solution to the problem.

A solution to this problem has been found through deeper insight into the physics of the laser ablation process. It was proposed to use for ablation picosecond or femtosecond laser pulses delivered on a target with a repetition rate of several tens of megahertz [31, 32]. The method was coined “ultrafast laser ablation” due to the combination of short laser pulses with a very high repetition rate. A single short low-energy pulse evaporates very few hot atoms per pulse, thereby inhibiting the condensation of droplets during fast nonequilibrium expansion. To compensate for the reduced ablated mass per pulse, high pulse repetition rates are then used to achieve a high averaged deposition rate. The application of the ultrafast laser ablation (UFLA) method for deposition of thin films has resulted in atomic surface quality films of diamondlike carbon [31, 32], with the total elimination of macroscopic particles from the film surface. Recently As_2S_3 chalcogenide optical films [34] have been produced with similar surface quality and high-volume homogeneity.

Complex nanoclustered networks of carbons were formed by evaporating a glassy carbon target in an argon-filled chamber. It was discovered that with the appropriate adjustment of the parameters of ablated flow and pressure of the ambient gas, the formation of new structures of a known material with unexpected properties results. For example, a new form of carbon, a cluster-assembled paramagnetic carbon nanofoam, was produced at an argon pressure above

0.1 Torr [37]. Conversely, at an argon pressure of 300–500 Torr, carbon nanotubes can be formed [28–30].

Recent developments clearly showed that a better understanding of basic physics and chemistry at all stages of the nanocluster formation process allowed the implementation of new methods for the prediction and control of this process. Using laser ablation, an atomized flow of any material with a controlled and predictable ablation rate, density, and temperature can be produced. The minimum number of particles ablated by a short-pulse (100 fs) laser is now reduced to $\sim 10^{11}$ atoms. This is comparable to the number of atoms in a cubic micrometer of a conventional solid. This is an important step toward the ultimate atom-to-atom attachment mode of nanocluster formation.

The research field of nanoscience and nanotechnology is a multidisciplinary one, in which the different areas of physics and chemistry overlap. In this review, we try to present a unified view of nanocluster formation by lasers, combining experimental results, theory, and simple models. The references were carefully selected to be guides in a vast sea of published papers, with emphasis on the most important topics and achievements. Therefore, the reference list is by no means exhaustive and reflects the views of the authors.

The review is organized as follows. First, we describe the lasers available for the ablation of different materials, the types of experimental installations for nanocluster production, and *in-situ* and *ex situ* diagnostic methods for observing cluster formation conditions and their structural and electronic properties (Section 2). Then we give a brief account of laser–matter interaction physics, with emphasis on the simple scaling that allows the prediction and interpretation of the experimentally observed ablation rate and plume parameters (Section 3). The processes of thin amorphous film formation and composite formation on a substrate are considered in Section 4. Laser plume–ambient gas interaction, the conditions for the formation of different nanostructures, and mechanisms for cluster formation are the topics of Section 5. In Section 6, the formation of cluster-assembled films and cluster networks is considered. Finally, we discuss the perspectives of laser ablation for the controlled production of nanostructures and the possibilities for scaling this method for industrial applications.

2. CLUSTER FORMATION BY LASER ABLATION: EXPERIMENTAL INSTALLATIONS AND DIAGNOSTIC METHODS

In this section, we describe the experimental installations for the formation of different nanoclusters in which a laser is used for ablation of a target to produce a flow of hot atoms. The general principles for the design of these installations are the same. The laser hits a target, ablates it, and produces a hot atomic flow in an expanding plume. This flow then interacts with atoms of noble gas in the chamber where the nanoclusters are formed. Depending on the laser parameters and on the kind of nanocluster to be formed, additional components, such as a furnace, diagnostic tools, etc., complement the major parts of the installation.

First, we briefly describe the lasers available for material ablation and nanocluster formation. Then we present the typical experimental installations used for different nanocluster formation. Finally, the experimental techniques for the *in-situ* diagnostics of cluster formation conditions and for the *ex situ* characterization of the final product are described.

2.1. Lasers

For ablation of materials, a variety of lasers is now available, with wavelengths ranging from 0.15 to 10 μm and with pulse durations spanning from several tens of femtoseconds up to continuous wave mode operation (cw lasers). The pulse repetition rate ranges from several Hertz to 100 MHz. With these lasers, the evaporation and atomization of any material is possible. Commercially available solid state Nd:YAG (fundamental wavelength, $1\omega = 1064\text{ nm}$; second harmonic, $2\omega = 532\text{ nm}$), Ti:sapphire lasers ($1\omega = 800\text{ nm}$; $2\omega = 400\text{ nm}$), along with XeF (353 nm), XeCl (308 nm), KrF (248 nm), ArF (193 nm), and F_2 (153 nm) excimer gas lasers with pulse durations of 10–30 ns, energy per pulse 0.5–0.3 J, and repetition rates of 10–30 Hz, are conventionally used in many experimental installations [15, 18, 26]. Recently subpicosecond lasers (pulse duration, 50 fs to tens of picoseconds) with high repetition rates of 10 kHz–100 MHz have been demonstrated to be very efficient for target ablation and nanocluster production [31–33].

The “state of the art” powerful Nd:YVO laser, newly developed at the Australian National University, can operate over a wide range of wavelengths, intensities, and repetition rates in the megaHertz range. This laser provides a flexible tool for producing an ablated flow of hot atoms of any material with a controlled temperature and ablation rate. It can be used for high repetition rate laser ablation and for the formation and deposition of different nanostructures. The laser generates 12-ps pulses with variable repetition rates of 1.5, 2.6, 4.1, and 75 MHz in the first (1.064 μm) and second (532 nm) harmonics at an average power of 50 W [38]. Further updating to generate in the third (355 nm) and forth (266 nm) harmonics is in progress. A variable repetition rate was achieved by extension of the laser cavity using a multipass cell to increase the cavity length up to 100 m. The time gap between consecutive pulses is from 15 to 750 ns. The laser produces a continuous flow of hot atoms with an ablation rate of $\sim 10^{20}$ atoms/s. This means that the mixture of the ablation plume and the ambient gas (usually argon) cools down slowly between the pulses, and the temperature of the mixture oscillates around the equilibrium level during the formation process [39].

Therefore, the temperature and atomic density in the nanocluster formation zone are controlled entirely by the tunable laser parameters: pulse duration, energy per pulse, and repetition rate. The principal scheme of this laser is presented in Figure 1.

Several important parameters, such as pulse duration, wavelength, pulse repetition rate, and laser fluence (J/cm^2) and intensity (W/cm^2), should be defined in order to choose an optimum laser for the ablation of a particular target and for cluster formation. First, the absorbed energy density

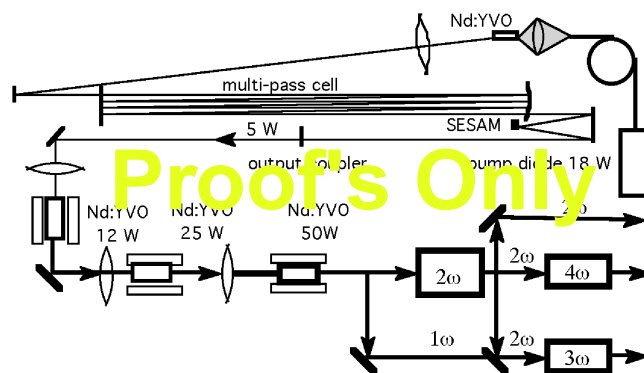


Figure 1. Principal scheme of a new powerful Nd:YVO laser installation at the Australian National University. The laser generates 12-ps pulses with variable repetition rates of 1.5, 2.6, and 4.1 MHz in the first (1.064 μm), second (532 nm), third (355 nm), and forth (266 nm) harmonics. It can be used for high repetition rate laser ablation and deposition of any material for the formation of different nanostructures under conditions controlled by flexible laser parameters.

delivered to the target should exceed the ablation threshold, which is in the range of 1–2 J/cm^2 for the majority of materials, and it can be defined for any material, as explained below in Section 3 [31]. The laser intensity and wavelength should be chosen appropriately to ensure efficient absorption of the laser radiation. Second, the molecular content and ionization state of the plume depend on the laser intensity distribution in time during the laser pulse and in space across the focal spot on the target surface.

2.2. Experimental Installations

2.2.1. Installation for the Production of Carbon Nanotubes

The use of laser ablation for nanocluster production was proposed by R. Smalley in 1983 [18]. The first installation used a commercial solid state low repetition rate laser with a noble gas flow through a tube placed in a furnace ($\sim 1200\text{ K}$) where single-walled carbon nanotubes were produced. Later Smalley and co-workers [27] proposed the use of two lasers for enhancing the mass production of carbon nanotubes. Their current installation [40] uses two Nd:YAG lasers for ablation of a graphite target containing the catalysts cobalt and nickel (1 at.% each). The target is maintained at 1473 K in a tube furnace in an argon atmosphere (100-sccm flow, 66.7-kPa pressure, 500 Torr). The lasers produce 8-ns, 300-mJ pulses, with a repetition rate of 10 Hz. The first laser operates at the fundamental wavelength of 1064 nm, while the second laser operates at the second harmonic of 532 nm and hits the target 50 ns after the first laser shot. The laser beams are adjusted to travel colinearly such that they overlap on the target. The weblike deposit contains the nanoclusters that were produced in the laser plume and in argon gas. The deposit is collected either on the brass water-cooled collector that is positioned at the end of a quartz tube just outside the furnace or on the quartz tube walls. The scheme of the installation is shown in Figure 2.

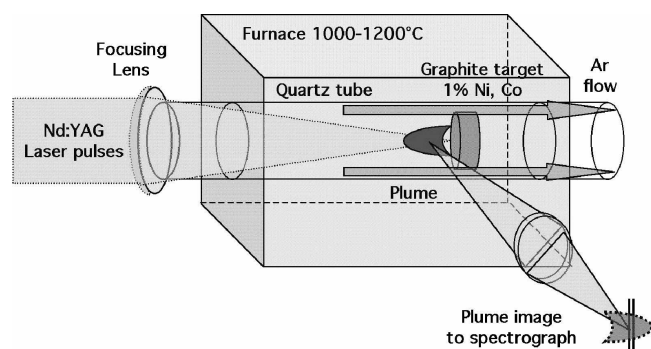


Figure 2. The first installation of single-walled carbon nanotube production proposed by R. E. Smalley [18]. The commercial solid state low repetition rate laser ablates a graphite target in a furnace heated to 1000–1200 °C with argon flowing through the furnace. Adapted with permission from [18], R. E. Smalley, *Laser Chem.* 2, 167 (1983). © 1983, ; [26], R. L. McCrory, “Nuclear Fusion by Inertial Confinement” (1999). © CRC Press; and [37], A. V. Rode et al., *Appl. Phys. A (Suppl.)* 69, S755 (1999). © 1999,

2.2.2. Experimental Setup for Formation of Metal and Covalent Clusters

The second typical installation is the so-called “laser vaporization cluster source” [1–3] that is used for production of metal and covalent clusters. In these devices, the clusters are also produced by the interaction of an ablated plume with the flow of a noble gas in the interaction chamber. The cluster flow is then released through a nozzle into a channel where mass (size) selection of clusters is performed. The flow of size-selected clusters is then deposited on a substrate. The scheme of a typical laser vaporization cluster source is shown in Figure 3.

2.2.3. Experimental Setup with High Repetition Rate Short-Pulse or Continuous-Wave Lasers: Formation of Cluster-Assembled Foams and Carbon and BN Nanotubes

The third type of installation is based upon commercially available powerful short-pulse high repetition rate lasers (see Fig. 4) [32, 33]. Short time intervals of 10–100 ns between the laser pulses lead to the overlapping of plumes produced by consecutive pulses. Proper tuning of both the laser intensity on the target surface and the pulse repetition rate allows one to control the temperature of the laser plume and noble gas mixture in the nanocluster formation zone, and a furnace for temperature control is not required. In installations described below, the laser parameters and scanning speed of the laser beam over the target surface are chosen to optimize the ablation rate, the temperature, and the molecular and ion states in the ablated plume.

Two high average power, high repetition rate Nd:YAG lasers ($\lambda = 1.064 \mu\text{m}$) were used for laser ablation of a carbon target and for deposition experiments [32]. One laser produced 42 W in 120-ns-long pulses with a variable repetition rate in the range of 2–25 kHz. This laser created an average intensity of $\sim 2 \times 10^9 \text{ W/cm}^2$ at the focal spot $S_{\text{foc}} = 1.6 \times 10^{-5} \text{ cm}^2$ on the target, or an energy density

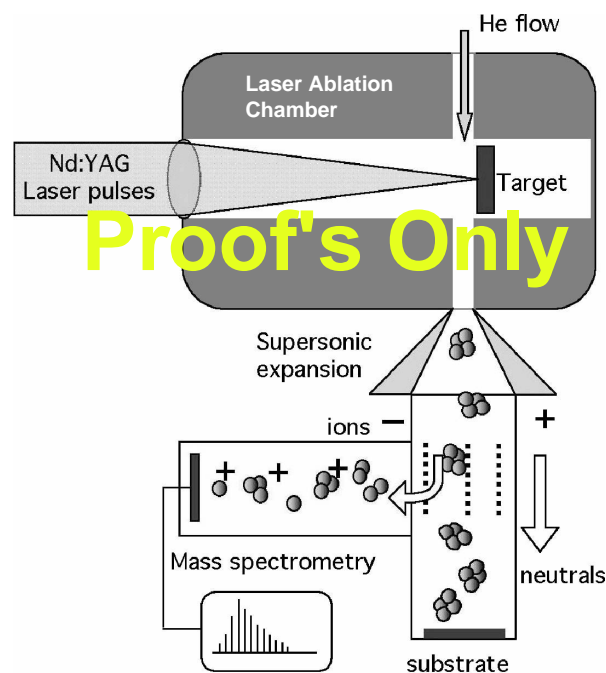


Figure 3. The scheme of a laser vaporization cluster source device that is used for the production of metal and covalent clusters, cluster-assembled film deposition, and mass spectrometry analysis. Adapted with permission from [1], K. Sattler, Ed., “Cluster Assembled Materials,” Vol. 232 (1996). © 1996, Trans Tech Publications Limited; [2], W. A. de Heer, *Rev. Mod. Phys.* 85, 611 (1993). © 1993, ; [3], P. Milani and S. Iannotta, “Cluster Beam Synthesis of Nanostructured Materials” (1999). © 1999, Springer-Verlag.

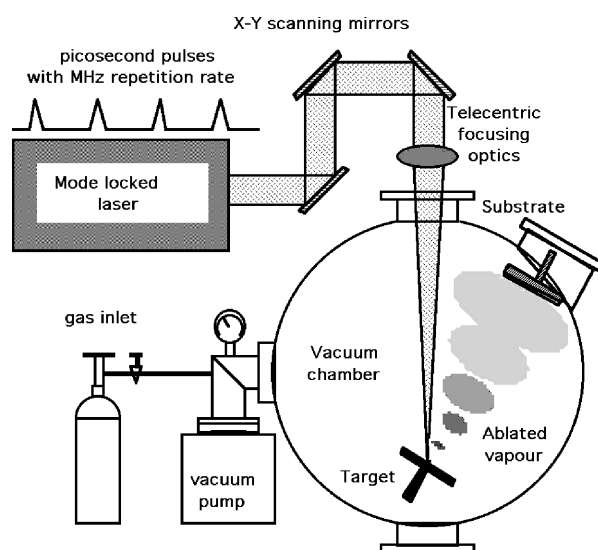


Figure 4. Schematic of the installation used for the formation of nanoclusters (carbon and boron nitride nanotubes) and nanoclustered materials (magnetic carbon nanofoam) in Ar at constant pressure with the use of high repetition rate short-pulse lasers. This installation is equipped with a powerful new laser [38] which allows the choice of all laser parameters: intensity, repetition rate, wavelength, etc., in order to obtain optimal conditions for the formation of the desired nanocluster.

in excess of 100 J/cm^2 . The second one was a 25-W 60-ps mode-locked laser with a repetition rate of 76 MHz. Note that the period between the consequent pulses in this laser comprises only 13.2 ns. An intensity of $\sim 3 \times 10^9 \text{ W/cm}^2$ was produced at the focal spot $S_{\text{foc}} = 1.8 \times 10^{-6} \text{ cm}^2$ with this laser [32].

2.3. *In-Situ* Characterization of Cluster Formation Conditions

2.3.1. Ablation Rate: The Feedstock for Cluster Formation

The rate of supply of hot atoms in the cluster formation zone depends on the laser ablation rate. This rate is conventionally measured by the target mass loss averaged over many laser pulses. This measurement provides an immediate check on how close the laser parameters are to those required for optimum evaporation. Indeed, the mass evaporated per single pulse can be estimated as the absorbed laser energy divided by the energy of evaporation per unit mass for a particular material. For example, if all the absorbed laser energy could be spent in evaporation, that is, spent only on breaking bonds, then 0.5 J of laser energy absorbed in a carbon target with the energy of vaporization at 30.4 kJ/g would result in ablation of $1.64 \times 10^{-5} \text{ g}$ of the target mass. However, the absorbed energy also goes into heat and shock waves in the target and in the kinetic and thermal energy of the ablated species.

Given optimum laser parameters, the ablation rate was found and measured in experiments with an Nd:YAG laser ($\lambda = 1.064 \text{ }\mu\text{m}$; pulse duration, $t_p = 120 \text{ ns}$; energy per pulse, $\sim 3 \text{ mJ}$ at 10 kHz) [32]. The evaporation rate by Rode et al. [32] was deduced from the volume V_{evap} of the evaporated conelike crater on the target surface, measured with both an optical microscope and a scanning electron microscope for a given number of pulses. For a single laser pulse the measured rate comprises 5.6×10^{14} particles/pulse (or $0.01 \text{ }\mu\text{g/pulse}$). Note that the measured differential rate $R_{\text{evap}} = (1.4 \pm 0.2) \times 10^{26} \text{ atoms/(cm}^2\text{/s)}$ qualitatively complies with the theoretical estimate of $10^{27} \text{ atoms/(cm}^2\text{/s)}$ [31]. One can easily note the importance of the high repetition rate laser. For the 10-kHz repetition rate by Rode et al. [32], the ablation rate comprises 10^{-4} g/s . In this case, the carbon feedstock into the nanocluster formation zone amounts to $5.6 \times 10^{18} \text{ particles/s}$.

A similar evaporation rate per pulse was observed in experiments where an XeCl excimer laser ($\lambda = 308 \text{ nm}$; repetition rate, 10 Hz ; $t_p = 17 \text{ ns}$) was used for the ablation of graphite [41]. The ablation rate decreased after 100 laser pulses per single spot on the target surface.

A C–Ni–Co target was ablated by a single CO_2 laser single pulse (20 ms; average intensity, $1.3 \times 10^5 \text{ W/cm}^2$) in an argon atmosphere with the goal of carbon nanotube production [29]. The ablation rate was measured by the target weight loss of 0.1 mg after 10 laser shots, thus amounting to 10^{-5} g/pulse .

The influence of the scanning speed of a laser beam over the target surface on the evaporation rate also has to be considered. If the laser focal spot is kept at the same position on the target for several consecutive pulses, a crater is

produced in the target, and its depth increases with each successive pulse. At very high repetition rates, this leads to an increase in the density of the vapor in the crater. As a result, the laser light is likely to be absorbed in the vapor away from the solid target surface and consequently, the interaction regime changes to a less favorable one in terms of evaporation efficiency [42]. When the crater depth becomes comparable with the diameter of the focal spot, the ablation rate drops in comparison to the single pulse regime. In a deep crater, the thermal losses from the vapor into the crater walls dominate the laser–target interaction process.

2.3.2. Emission Spectra of the Plume and Ambient Gas Mixture

Transient Temperature The emission spectrum of the target surface and the laser plume consists of two easily distinguished parts: one is continuous radiation, and another is line radiation. The average temperature of the mixture of the ablated plume with ambient gas can be found by fitting the continuous radiation spectrum with Planck's radiation law. Line radiation allows one to identify the molecular and ion content in the plume and to estimate the temperature and the level of ionization.

The comparison of the line radiation with known spectral lines allows for the identification of the molecular content of a plume. For example, time-integrated, space-resolved, target surface and plume temperatures were measured by Rode et al. [32] for a carbon target ablated by 10-kHz 120-ns laser pulses in a vacuum. The continuous radiation in the 600- to 800-nm range fits well with the Planck spectrum, with the temperature in the range of 2500 to 3500 K.

Single-wall carbon nanotubes were grown by ablation of a carbon–cobalt–nickel target with a Nd:YAG laser ($1.064 \text{ }\mu\text{m}$, 300 mJ/pulse, 8 ns pulse width) in argon gas in an oven heated to $760\text{--}1100 \text{ }^\circ\text{C}$ [43]. The transient temperature of the carbon plume diffusing through the argon was estimated by Puretzky et al. [43] by fitting the measured blackbody radiation spectrum to Planck's law. The temperature of the carbon–argon gas mixture changes from $3500 \text{ }^\circ\text{C}$ at 0.1 ms to $1488 \text{ }^\circ\text{C}$ at 1 ms after ablation. It decreases to the oven temperature during the next 4 ms.

A similar procedure of fitting the continuous emission spectra to the Planck function by Kokai et al. [29] gives the temperatures for a carbon cluster–argon mixture in the range $3410\text{--}3540 \text{ K}$. Note that in this case, the single-wall carbon nanotubes were synthesized by ablation of a C–Ni–Co target by a 20-ms CO_2 laser single pulse ($\lambda = 10.6 \text{ }\mu\text{m}$; peak power, $\sim 1 \text{ kW}$; average intensity, $1.3 \times 10^5 \text{ W/cm}^2$) in an argon atmosphere. Thus, under all seemingly different conditions, the temperature in the formation zone for carbon nanotube formation is around $\sim 3000 \text{ K}$.

Molecular Content of a Plume Determined by Spectroscopic Measurements

The carbon target was ablated by relatively long 120-ns laser pulses at a 10-kHz repetition rate at an intensity of $1\text{--}3 \times 10^9 \text{ W/cm}^2$ [32]. The analysis of the line radiation spectrum of a carbon plume in a spectral range below 400 nm by Rode et al. [32] revealed that there is rather weak radiation from neutral carbon at 248 nm (the first excitation line for carbon) along with the

intense lines corresponding to singly ionized and doubly ionized carbon. The temperature estimates led to high values of 1.5–6 eV in the plume.

The emission spectrum of a carbon–argon mixture was recorded by Arepalli et al. [40] in the spectral range of 300–650 nm. The spectral features were identified as emission of a Swan system from C_2 and a Comet Head system relevant to the presence of C_3 . Comparison of the computed spectra to the measured excitation spectra allowed estimation of the vibration temperature in the range of 2500 to 4000 K. The temperature measurement results clearly demonstrate that the ionization time in the plume should be considered along with the intensity of the laser radiation on the target surface for predicting the plume temperature in the cluster formation zone [44].

2.4. In-Situ Characterization of the Cluster Size (Mass)

2.4.1. Cluster Mass Abundance Spectra

Clusters are formed as a result of interaction of the laser plume with noble gas in a cluster nucleation chamber (Fig. 3). The clusters then flow through a nozzle to the channel leading to the deposition chamber, where a substrate is located [2, 3, 45].

Cluster size (mass) distribution is conventionally determined by a time-of-flight method in a double-field configuration (see, for example [1–3] and references therein). In this method, the ionized clusters are deflected in the applied electric field and then separated in accordance with the charge/mass ratio. When neutral clusters are produced, a separate short-wave laser is used to ionize the neutral clusters, and then they are deviated by an applied electric field and analyzed with a spectrometer. The photon energy of the short-wave laser is chosen to be slightly larger than the first ionization potential of cluster material to assure that only single charged clusters will be produced. The mass abundance spectra have characteristic maxima at “magic numbers” which correspond to the most stable remarkable atomic structures, such as fullerene (C_{60}), cobalt and nickel icosahedra, aluminium octahedra, or metal clusters with closed electronic shells.

The most spectacular mass distribution (or, distribution of number of atoms per cluster) of carbon clusters produced by laser ablation of graphite was obtained by Rohlfing et al. [45] (see Fig. 5). The distribution is bimodal and the highest cluster intensity in the second peak corresponds to the famous fullerene, C_{60} , cluster. A typical mass resolution in this method, $M/\Delta M$, commonly stands between 100 and 1000, but it can be improved up to 30,000 [1].

2.4.2. In-Situ Absorption Spectroscopy of Carbon Nanoparticles: Average Cluster Size

In order to estimate the size of carbon clusters in the plume–ambient gas mixture absorption spectroscopy was used by Puretzky et al. [46]. The short (35–77 nm) single-wall carbon nanotubes were formed using nanosecond Nd:YAG laser ablation of a C–Ni–Co target inside a high-temperature

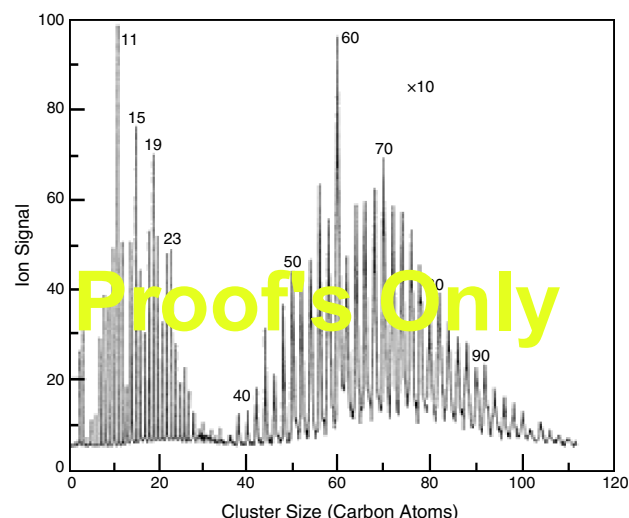


Figure 5. Mass distribution of carbon clusters, containing n carbons, created by the laser ablation of graphite. Reprinted with permission from [51], D. Goldberg et al., *Carbon* 37, 1858 (1999). © 1999, Elsevier Science.

(760–1100 °C) argon-filled oven. The light from a pulsed Xe lamp passed through the ablated plume in the oven, and then the extinction spectrum was measured. The set of extinction spectra was also calculated on the basis of Mie theory for the scattering and absorption of light on spherical particles of a relatively large size (diameter $d > 0.05\lambda$ where λ is the wavelength of the scattered radiation) [47]. For such particles, the extinction spectra are sensitive to the particle size. Comparison of calculated and measured spectra has shown that good fit of the experiment to the theory is obtained for the cluster diameter of 80 nm. This means that 1 ms after the ablation, when the spectra were measured, the carbon atoms have already aggregated into large clusters.

2.4.3. Imaging of a Plume Diffusion Through the Ambient Gas: Onset of and Time for Cluster Formation

Carbon nanotubes are conventionally formed through interaction of a laser-ablated plume of a carbon–cobalt–nickel target with a noble gas, which fills the experimental chamber. However, it is still unclear how long it takes for nanotube formation, when the growth process starts and ends, and what the conditions (temperature and density) in the formation zone are. Recently several experimental groups published results clarifying some of the stages in the cluster building process.

Single-wall carbon nanotubes were synthesized by ablation of a C–Ni–Co target with 20-ms pulses from a CO_2 laser (1 kW peak power; average intensity, 1.3×10^5 W/cm²) in an argon atmosphere [29]. A high-speed video imaging technique was applied to record the expansion of the ablating plume. The authors observed that the moment when the carbonaceous material in the expanding plume became visible was 3 ms after the beginning of the laser pulse. This moment can be qualitatively identified as the moment when

the number of big clusters became sufficient to make the absorption in the plume visible. The expansion velocity of the plume in the argon atmosphere (the velocity of propagation of the diffusion front) was measured to be $\sim 10^3$ cm/s as estimated from the plume images at 1.7 and 3.3 ms.

Puretzky et al. [43] suggested that the time of nanotube growth is related to the time dwelt by the plume in the region of the furnace where the temperature is almost uniform. In order to measure this time dwell, the propagation of the laser-ablated C–Co–Ni plume diffusing through an Ar atmosphere at 500 Torr was registered *in-situ* by measuring the scattered light from a time-delayed probe laser beam (XeCl laser, 308 nm, 30 ns, 6 mJ/cm²) [43]. By measuring the velocity of plume diffusion, the above dwelling time or formation time can be estimated. This time ranges from 15 to 120 ms. The authors [43] also measured the length distribution among nanotubes created under slightly different temperature conditions. The maximum length distribution of the nanotubes formed ranges from 35 to 77 nm. One can relate the above growth time to the corresponding nanotube length and obtain the growth rate for the nanotubes, which ranges from 0.6 to 5.1 $\mu\text{m/s}$. The measured growth rate measurements are in agreement with simple kinetic estimates of the single-walled nanotube formation rate under different thermal conditions and similar Ar pressure, which are in the range of 0.5–100 $\mu\text{m/s}$ [48].

It is interesting to note that the measured velocity of the leading (sharp) edge of the diffusing plume in [43] changes abruptly at ~ 3 ms, decreasing from $\nu_D = 8$ to 0.76×10^3 cm/s. This velocity is directly related to the average diffusion velocity, $D = l\nu/3$, of carbon atoms in the argon atmosphere (here $l = (n\sigma)^{-1}$ is the cluster mean free path; n is the number density of particles in the formation zone (mainly argon atoms); $\sigma \sim r_{\text{cluster}}^2 \sim N^{2/3}$ is the cross section for cluster–argon collision, where r_{cluster} is the cluster radius and N is the number of atoms in the cluster). The velocity of a cluster decreases as the cluster mass increases since $\nu \sim (T/Nm)^{1/2} \sim N^{-1/2}$. Therefore, the diffusion velocity depends on the cluster size according to $D \sim N^{-7/6}$ [48]. The distance traveled by the diffusion front as it was measured in the experiment can be expressed as $R = (Dt)^{1/2} = \nu_D t$. Therefore $D \sim (\nu_D)^2 t$. The cluster size grows as the diffusing front propagates through the cluster formation zone. Thus, in accordance with the plume propagation measurements in [43] after 3 ms, the number of particles in an average cluster increases ~ 100 -fold.

2.5. Ex-Situ Characterization of Individual Clusters and Cluster-Assembled Films (Foams): Structural and Electronic Properties

In this section we describe the diagnostic methods for *ex situ* characterization of structural and electronic properties of individual nanoclusters and cluster-assembled materials.

2.5.1. Electron Microscopy

A very powerful tool for studying the electronic and structural features of nanoclusters is electron microscopy, with which imaging of the electron beam scattering on and

transmission through the studied structure as well as the interference and diffraction patterns can be investigated. Electron microscopy allows the identification of subtle structural features of complicated individual nanoclusters and nanocluster networks. The images of single-wall carbon nanotubes were obtained by using scanning tunneling microscopy [49, 50]. This technique gives atomically resolved lattice images of relatively high contrast. However, there are difficulties in observing such delicate features as the chirality of nanotubes by using this technique. Recently, high-resolution transmission electron microscopy, operating in the imaging mode, was used for characterization of single-walled carbon nanotubes and nanotube bundles produced by the laser ablation technique [51]. A high-resolution transmission analytical electron microscope, the JEM-300F (JEOL) equipped with a 300-keV field emission gun (NIRIM Tsukuba, Japan), was used for these observations. The microscope has a theoretical spatial resolution limit of 0.17 nm. In reality, lattice fringes of 0.21 nm were resolved in the “core” region of a single-walled nanotube, as is seen in Figure 6. Considering the orientation and contrast of these fringes, a researcher is able to observe and estimate such subtle nanotube characteristics as chirality (or helicity) [51].

2.5.2. Raman Spectroscopy

The Raman scattering technique is a powerful tool for determining the structural features of different crystalline structures, nanoclusters, and nanomaterials. Comparison of the known Raman spectra of a bulk crystalline material to that of the nanoclustered allows the determination of a transition to a nanostate where quantum confinement effects can be observed. The Raman spectra of carbon nanoclustered materials are usually compared to crystalline diamond and graphite lines. Diamond has a very sharp peak at 1330 cm^{-1} , and graphite is characterized by two broad peaks at 1400 cm^{-1} (D-peak) and 1600 cm^{-1} (G-peak) [52]. Amorphous carbon (a-C), regardless of the way it is produced, tends to have a broad single asymmetric peak with a maximum around $1500\text{--}1550\text{ cm}^{-1}$ [52, 53].

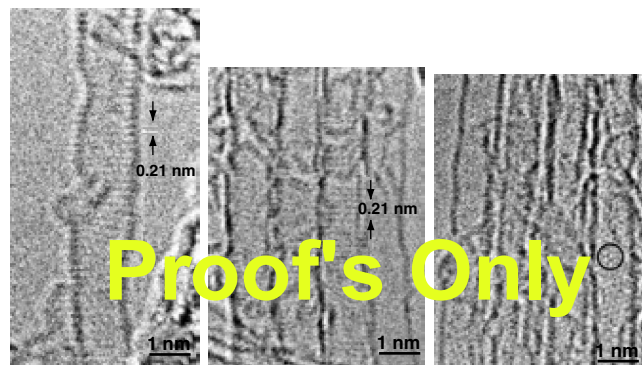


Figure 6. Atomically resolved high-resolution transmission electron microscope (HRTEM) images of an individual single-wall carbon nanotube in a bundle (a) and an isolated tube (b) exhibiting 0.21-nm fringes in the core region in agreement with a “zigzag” arrangement of atoms. Reprinted with permission from [51], D. Goldberg et al., *Carbon* 37, 1858 (1999). © 1999, Elsevier Science.

Raman spectra of the carbon nanofoam measured with an excitation wavelength of 632.8 nm showed two separated broad peaks centered at 1341–1353 and at 1569–1579 cm^{-1} , which were attributed to graphitic sp^2 bonding [54]. The detected peaks at 1350 and 1580 cm^{-1} were assigned to disordered and ordered carbon phases, respectively, and the samples were described as glassy carbon with very little order.

A resonant Raman scattering process on single-wall carbon nanotubes was observed with the laser excitation wavelength varying from 514.5 to 1320 nm [55]. The resonance results from the one-dimensional quantum confinement of the electrons in the nanotube. It was shown theoretically and later confirmed experimentally [56] that depending on the symmetry and diameter of the carbon nanotubes, they can be either metallic or semiconducting. These quantum size effects manifest themselves in the Raman scattering signal from the nanotube vibrational modes. In [55] carbonaceous structures were produced by laser ablation. These nanotubes with a very narrow diameter distribution were separated through a long purification procedure, including a microfiltration technique to remove most of the carbon nanoparticles which were also produced in the process.

According to theory [56], nanotubes are described by two indices (n, m) . These indices (n, m) define the atomic coordinates for the one-dimensional unit cell of the nanotube. The tube with $n \neq m \neq 0$ has a chiral symmetry. The achiral tubes ($m = 0$, or $m = n$) are divided into two subclasses: tubes with $(n, 0)$ are referred to as “zigzag” tubes and tubes with (n, n) are referred to as “armchair” tubes. The Raman data were analyzed assuming only the armchair symmetry for the studied tubes because the previous calculations have shown that chiral tubes exhibit very few Raman-active modes in the range 400–1500 cm^{-1} .

The theory predicts a strong diameter-dependent Raman line: 206 cm^{-1} for (8, 8) nanotubes with diameter $d = 10.85 \text{ \AA}$ and 150 cm^{-1} for (11, 11) nanotubes with diameter $d = 14.927 \text{ \AA}$. Using 514.5-nm laser excitation, a strong broad line was observed at 186 cm^{-1} . This line associated with a randomly oriented mixture of nanotubes with diameters corresponding to (n, n) tubes with n ranging from 8 to 11. Thus, the Raman observation allows a reasonable estimation of the average diameter of nanotubes in the sample.

It was also observed [55] that the Raman spectrum (intensity and positions of the peaks) strongly depends on the laser excitation frequency. The redistribution of the spectral intensity as a function of the excitation wavelength is an indication of unusual resonant Raman scattering. Resonant scattering occurs when the energy of the incident photon matches the energy difference in an electronic transition due to optical absorption. It is now well known that starting from some small dimension on the nanometer scale (a certain diameter of nanotube or nanocluster), the energy difference between the electronic states responsible for the optical absorption increases when the nanocluster diameter decreases. This effect is often referred to as the quantum size effect or as a one-dimensional quantum confinement phenomenon. For a large diameter, the character of the electronic states is essentially independent of the tube diameter, so the Raman spectrum should be very close to that for a flat graphene sheet and should be independent of the

excitation frequency. The experimental observations and calculations of a Raman spectrum presented by Rao et al. [55] provide strong evidence of a diameter-dependent Raman effect that is a consequence of quantum confinement in single-wall carbon nanotubes with diameters of 10–15 Å.

2.5.3. Electron Energy Loss Spectroscopy

The character of the bonding in an individual nanocluster or in a nanocluster-assembled material can be investigated using the electron energy-loss spectra (EELS) technique [57]. For example, in carbonaceous materials the important characteristic of the electronic structure is the ratio of sp^2 hybridized bonds (signature of graphite) to sp^3 bonds (signature of diamond). This ratio $\text{sp}^2/(\text{sp}^2 + \text{sp}^3)$ in carbon nanofoam was investigated by the EELS technique [37]. The EELS spectra were analyzed using a GATAN 666 parallel electron energy-loss spectrometer (PEELS). PEELS spectra were collected by two methods. First, a number of different regions of laser-produced carbon nanoclusters were chosen and five different spectra were collected from around each region. In the second method, in-house software was used to collect a number of spectra along a chosen straight line across the nanocluster. This method allowed one mapping of the variation of sp^2 bonding across a single cluster with 1-nm spatial resolution [58]. The mapping of a 6-nm carbon cluster, which is a typical structural unit of the nanofoam, revealed that the carbon atoms inside the clusters have predominantly sp^2 bonding, while at the cluster boundaries sp^3 “diamond-like” bonding prevails.

2.5.4. Surface Area Measurements for Nanocluster-Assembled Materials

Nanocluster-assembled materials usually have a porous, sponge-like or foam-like structure. One of the characteristics for such materials is the characteristic surface area, that is, the area of the inner pores for the unit weight of material. The multipoint Brunauer–Emmett–Teller (BET) method [59] for surface area measurements is commonly used to measure this parameter.

Using this method, the surface area measurements for carbon nanofoam produced by the ultrafast laser ablation of graphite were performed using a Micromeritics Gemini II 2375 surface-area analyzer [37]. About 100 mg of nano-material was placed into a sample holder and first outgassed at 120 °C under a nitrogen flow and immersed in liquid nitrogen. The measurements showed that the surface area of the nanofoam is in the range of 300–400 m^2/g . Detailed studies of the desorption of the nitrogen from the foam can be made using the BJH method [60], which calculates the pore volume distribution. The analysis of nanofoams formed at different argon pressures demonstrated that all foam samples have essentially constant pore volume, with no evidence of a preferred pore size.

2.5.5. Small-Angle X-Ray Scattering

Small-angle X-ray scattering data have been found useful for analysis of the fractal dimensions of aerogels, carbon nanofoam [37], and nanoclusters [1–3]. X-rays from a conventional Cu X-ray source were collimated with standard

Guinier optics onto a carbon nanofoam sample to reveal its structural features. The scattered radiation has been collected on a home-built camera [37]. According to Schmidt [61], fractal structures of fractal dimension d give rise to a power law decay of the scattered intensity $I(q) \sim q^{-d}$, where q is the scattering vector. The exact location of this power law regime on the q scale is in practice delicate. However, it is possible in some cases to identify this functional form over a reasonable q range. Rode et al. [37] found the power law to be valid in a range of $0.1\text{--}0.4 \text{ \AA}^{-1}$, leading to an estimation of the fractal dimension of 2.4. This means that the atomic arrangement in space lies somewhere in between homogeneous two-dimensional sheets and three-dimensional (3D) volumes.

2.5.6. Measurement of the Bulk Density of Cluster-Assembled Materials

A convenient method for determining of the bulk density of cluster-assembled materials (foams, aerogels, sponges, etc.) is Rutherford backscattering [62]. The bulk density of the carbon nanofoam deposited on a silicon substrate [37] was determined from 2-MeV He^+ ion backscattering measurements. The area density of the sample was deduced from the energy width of the carbon peak and the energy shift of the silicon edge, and the thickness of the foam sample was obtained from the scanning electron microscope images (see Fig. 7), giving the density of the foam as $2\text{--}10 \times 10^{-3} \text{ g/cm}^3$.

3. HOT VAPOR (PLASMA) PRODUCED BY LASER ABLATION

In this section we underline the main physical features of laser–matter interaction and formation of an evaporated plume of hot vapor and plasma. The simple and self-consistent procedure allows the choice of the proper combination of laser and material parameters to design an experiment for producing a plume with the desired parameters, for example, to produce an atomic flow by laser ablation.

3.1. Laser–Matter Interaction: Light Absorption and Ablation Threshold

In order to remove an atom from a solid by means of a laser pulse one should deliver energy in excess of the binding energy ε_b of that atom (the energy of evaporation per atom).

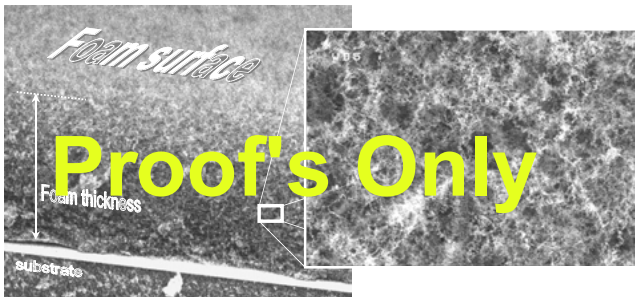


Figure 7. Scanning electron microscope images of a $100\text{-}\mu\text{m}$ -thick nanofoam assembled from carbon nanoclusters and deposited on a silicon substrate.

Therefore, to begin with, efficient absorption of the laser energy is necessary. The ratio of the absorbed energy flux to the incident laser flux, or the absorption coefficient, depends on the material properties and on the intensity and wavelength of the laser.

Absorption coefficients for different materials and for various wavelengths can be found in the literature [31, 63, 64]. To illustrate spectral dependencies we present simple estimates for the absorption coefficient for metals. The laser field penetrates into a solid at the skin depth, l_s , which in metals is much smaller than the wavelength of the laser, $l_s \ll \lambda$. The skin depth, $l_s = \frac{c}{\omega k}$, is conventionally expressed through the imaginary part of the refractive index, k , and the laser frequency, ω [63]. One can show that the absorption coefficient is given by $A \approx \frac{4\pi l_s}{\lambda}$ [65]. As can be seen, the use of short wavelength lasers is preferable for good absorption. Electrons absorb the laser energy at a distance comparable to the skin depth. Suppose that the laser intensity distribution, I_0 (W/cm^2), over the focal spot diameter and during the pulse time, t_p , has a “tophat” profile. The absorbed laser energy per unit area F (J/cm^2) is expressed as $F = AI_0 t_p$. This quantity is called the absorbed fluence.

The absorbed energy is confined in the electrons, and therefore, the maximum electron temperature at the end of the laser pulse is proportional to the absorbed laser fluence as

$$T_e = \frac{2F}{3n_e l_s}$$

where n_e is the number density of free electrons in the metal. Finally the hot electrons transfer their energy to cold ions, and the electron and ion temperature T_i equilibrates, such that $T_e = T_i$. The ions can leave the solid (or to be evaporated) if $T_i > \varepsilon_b$. Now one can immediately obtain a relation between the laser fluence and material parameters needed to reach the ablation threshold $F_{\text{threshold}} = \frac{3}{2} n_e l_s \varepsilon_b$. A typical binding energy for the majority of solids is a few electron volts and therefore, the typical absorbed laser fluence for ablation threshold is around 0.5 J/cm^2 .

One can see that ablation by long or short laser pulses occurs under very different conditions. In order to ablate the same amount of material with a short pulse, one should apply a larger laser intensity approximately in inverse proportion to the pulse duration. For example, laser ablation with a 100-fs pulse requires the intensity to be above 10^{13} W/cm^2 [31–33, 65], while with 10-ns pulses, the same material is ablated at much lower intensities, $\sim 10^8\text{--}10^9 \text{ W/cm}^2$ [31]. The depth of material ablated per single short laser pulse is proportional to the skin depth, whereas in the case of long pulse ablation, the characteristic ablation depth is proportional to the heat conduction length per pulse $\sim (at_p)^{1/2}$, where a is the thermal diffusivity (cm^2/s) of the target material. Correspondingly, the number of particles evaporated per pulse differs by several orders of magnitude.

It has been shown [33, 65] that at laser intensities in excess of 10^{13} W/cm^2 , practically any target material is ionized during the subpicosecond pulse time. Following ionization, the laser energy is efficiently absorbed by free electrons due to

inverse Bremsstrahlung and resonance absorption mechanisms and does not depend on the initial state of the target. Consequently, the interaction of a laser pulse with both metals and dielectrics proceeds in a similar way. The efficient evaporation of dielectrics and the formation of atomic beams of ablated atoms is now possible using short and intense laser pulses. Since additional energy, ~ 10 eV/atom, is required for ionization, it is obvious that the ablation threshold for dielectrics must be higher than that for metals. Indeed, the experiments show that the ablation threshold for dielectrics is typically ~ 2 J/cm² [33].

3.2. Ablation Rate and Deposition Rate

The most efficient ablation will be achieved if all the absorbed energy is used in ablation only, and any losses and overheating of the plume are avoided. In this case, the instantaneous ablation rate (the ablation rate during the pulse) can be easily estimated as the absorbed laser intensity divided by the binding energy

$$(nv)_{\text{abl}} \approx \frac{AI_0}{\varepsilon_b} \text{ (atoms/cm}^2\text{/s)}$$

In fact this ablation rate is close to the experimentally measured value for the optimum ablation mode. This is the highest rate from all available ablation methods. The values for the instantaneous ablation rate span from 10^{32} atoms/cm²/s for short, ~ 100 -fs pulses, to 10^{27} atoms/cm²/s for the nanosecond pulses. The total number of atoms evaporated per single pulse with the total energy E_{las} is given by $AE_{\text{las}}/\varepsilon_b$. The laser energy per short pulse is in the order of $\sim \mu\text{J}$, while in the nanosecond pulses it reaches 1 J. Thus, the ablation rate per pulse, with the pulse duration ranging from nanoseconds to femtoseconds, is correspondingly $\sim 10^{12}$ – 10^{18} atoms/pulse. Taking into account the different pulse repetition rates (up to 100 MHz for the short pulses and 10–30 Hz for the long nanosecond pulses) one can see that the average flow of laser-ablated atoms is $N \sim 10^{19}$ – 10^{20} atoms/s near the ablation surface. This figure, along with the temperature and ionization state of the vapor, defines the initial conditions for the formation of new structures in a chamber.

Let us consider the use of the atomic flow for the deposition of thin films on a substrate placed at a distance d from the target in an evacuated chamber. The film growth rate for the formation of a film with a number density n_a is defined as $N/2\pi d^2 n_a$. Thus, taking the average target to substrate distance of 10 cm and the number density of solid 10^{23} atoms/cm³ the deposition rate for the formation of amorphous films with laser ablation can reach several tens of nanometers per second.

3.3. Criterion for the Full Atomization of Ablated Vapor

The phase state of the ablated vapors is determined by the conditions of evaporation, that is, it depends on the amount of laser energy absorbed in the ablating material. The energy delivered by a laser is spent on the breaking of interatomic bonds and on the kinetic energy of atomic expansion. If this kinetic energy is low, the vapor expands slowly, and therefore it can be condensed back near the target shortly after

the laser pulse termination. We shall determine the magnitude of the kinetic energy sufficient for keeping the plume expanding into a vacuum in a gas state of non-interacting atoms. One can estimate the energy threshold necessary to achieve full atomization of the ablated plume on the basis of thermodynamic arguments similar to those used for establishing the criterion for complete vaporization of a material in an unloading stage after the action of a strong shock wave [66]. In this case all the nonequilibrium processes related to the energy transfer to ions are assumed to be completed before the expansion begins. The target material after the termination of the pulse experiences adiabatic expansion.

The adiabatic expansion from a solid state to the gas state can be described by the conventional relation between the gas energy, pressure P , and gas volume, V , but with a volume-dependent exponent (so called the Gruneisen coefficient). In order to get the final stage of expansion as a gas state, the adiabatic curve in the PV plane must pass higher than the critical point, $P_{\text{cr}}, V_{\text{cr}}$, separating the states of a homogeneous phase (atomized vapor) from states with a mixture of phases (gas and condensed liquid droplets). Given these constraints, it can be determined that the energy delivered by the laser per ablated atom must be approximately three to four times larger than the binding energy. Therefore, the absorbed laser energy density necessary to transform the ablated material into an atomized vapor should exceed the ablation threshold in accordance with the condition $F > 4F_{\text{thr}}$.

3.4. Damage and Condensation Thresholds

If the total energy delivered by the laser is close to the binding energy, $\varepsilon_{\text{total}} \sim \varepsilon_b$, then a solid experiences only a small density decrease from the standard solid density of the target material. The pressure in the material is comparable to the bulk modulus. Therefore, the final state of the target affected by the laser at this energy level might be considered “damaged,” having cracks, flakes, etc. in the laser focal spot depending on the initial state of the target (such as the presence of defects, impurities, etc.). If the deposited energy is in the range $\varepsilon_b < \varepsilon_{\text{total}} < (3-4)\varepsilon_b$, then the final state of the expanding vapors may lie in the region of the pressure–volume parameter space where the mixture of phases is energetically favorable. The condensation of vapor into liquid droplets in a course of expansion in a vacuum may occur when the absorbed laser energy is within $F_{\text{thr}} < F < (3-4)F_{\text{thr}}$.

3.5. Ionization State and Velocity Spectrum of Ablated Ions

Ionization of a solid target material during the ablation process and the ionization of ablated vapors occurs due to processes of photoionization, multiphoton ionization, and ionization by electron impact (avalanche ionization) [66]. As ionization proceeds, the vapor is converted into a high-density plasma whose properties can eventually dominate the physics of the laser–vapor interaction. If the laser–matter interaction occurs at a high intensity, which is typical in ablation by femtosecond laser pulses, the full first ionization is completed during the first few femtoseconds at the

beginning of the laser pulse [65–68]. Afterward the interaction proceeds with the plasma. The energy distribution of the ions in the ablated flow appears to be non-Maxwellian. It can be roughly approximated as a two-bump distribution composed of the slow and fast parts. Experimental and theoretical studies have demonstrated that the energy distribution of outflowing ions is highly dependent on the ratio of the maximum intensity in the main laser pulse to the intensity in the prepulse (the so-called contrast ratio) [69]. It has been observed that for 100-fs laser pulses in the laser intensity range of 10^{14} – 10^{16} W/cm², the ion energies vary from 100 eV to 20 keV [69]. Therefore, the interaction of an ionized flow, either with an ambient gas in the chamber resulting in cluster formation or with a substrate leading to the formation of a nanofilm, proceeds in a different way, as has been confirmed by experiments which are discussed below. We should stress that all parameters of a hot atomic flow which affect the process of a nanocluster formation can be controlled and steered in a desirable manner.

4. FORMATION OF NANOCLUSTERS IN A VACUUM

The whole process of nanostructure formation can be separated tentatively into the following stages. First, laser-ablated atomic vapors (or plasma) are produced to form a plume. Then, the laser plume expands into a vacuum and cools in the experimental chamber. The nanostructure formation process (nucleation) is composed of vapor–vapor, vapor–filling gas, vapor–substrate, and cluster–substrate interactions. Finally, the resulting product is annealed and cooled. In this section, we concentrate on the processes of nanostructure formation, taking the parameters of ablated vapors (plasma) as the initial conditions. Then, we discuss the characterization of the structure produced and relate the structural and material features to the formation conditions resulting from vapor–gas–substrate coupling.

We start from the most studied process of thin film deposition in an evacuated chamber. Recently a huge variety of different structures were deposited by the laser ablation method including refractive and complex materials. The literature covering this topic comprises thousands of references [i.e., 70, 71]. Our goal in this review is to point out relations between the properties of the atomic beam, the ambient gas, and the conditions created in the chamber to the properties of the emerging nanostructure. Such relations, when properly understood, would allow the control and prediction of the formation process. Therefore, we concentrate on several structures where this relation has been at least partly revealed. We also mention recent achievements in the quality and in the efficiency of thin film deposition, which makes the pulsed laser deposition technique more attractive for industrial applications.

4.1. Deposition of Nanometric Films in a Vacuum

Laser ablation has been successfully used for thin film deposition during the last 3 decades with the use of conventional nanosecond, 10- to 30-Hz lasers [70–72]. However, due to

poor control over the laser beam parameters in these lasers, the surface quality (abundance of droplets) and material properties (for example, the sp²/sp³ bond ratio in carbon films) would differ from one laser installation to another with seemingly similar parameters. In addition, the deposition rate with lasers running at a repetition rate of 10–30 Hz was too low for most industrial applications.

The recent advent of short-pulse, high average power, high repetition rate lasers resulted in the elimination of these drawbacks of laser deposition. Progress in the understanding of the ablation process led to control over the pulse time shape (elimination of the prepulse), over the spatial distribution of the intensity across the laser focal spot (top-hat distribution), and over the temperature of the ablated ions. Now full control of the ablated plume parameters, at least in principle, can be provided. Future developments will determine whether it will be possible to make this process cost effective and to scale it to the industrial level.

4.1.1. Interaction of Hot Atoms with a Substrate in a Vacuum

Let us describe the succession of processes accompanying thin film deposition in a vacuum. We consider, for example, the flow of carbon atoms forming diamond-like carbon films on a substrate (conventionally the substrate is a silicon or silica) in a high vacuum, $P = \sim 10^{-6}$ – 10^{-7} Torr, which corresponds to a density of air molecules of $\sim 2 \times 10^9$ – 10^{10} cm⁻³. A short-pulse laser with a high repetition rate produces 10^{19} – 10^{20} atoms/s, which destroys the vacuum after several seconds of operation [32, 73–75]. Therefore, continuous chamber evacuation is necessary in order to maintain constant conditions during the long, 30- to 120-min deposition process. Continuous chamber evacuation at a rate of 2×10^3 liters/s maintains the number density of particles in the chamber at an approximately constant level of $n_a \sim 2 \times 10^{10}$ cm⁻³ [73]. Under these conditions, the mean free path for the particles (carbon atoms and air molecules) is $l \sim 1/n_a \sigma = 5 \times 10^4$ cm, assuming that the cross section of atom–atom collisions is $\sigma \sim 10^{-15}$ cm². Hence, one can suggest that there is no influence from any collisions in the chamber on the film formation process at the substrate and no cooling of the carbon atoms under this vacuum condition. Thus, the films of any material are formed due to direct vapor–substrate interaction at the vapor’s temperature, which approximately corresponds to the target surface temperature. Note that these conditions are appropriate for the formation of sp³ carbon bonds assuming $T > 10^3$ K. However, not all of the collisions between the ablated atoms and the substrate lead to the sticky attachment of an atom to the substrate. Some atoms can rebound from the substrate or from the chamber walls, cool down, and flow around the vacuum chamber [3, 73, 76]. Some small deposition of the ablated material on the rear side of the substrate may serve as direct experimental evidence of this effect.

Another important factor for deposited film formation is the pressure on the substrate during the film building process. This pressure consists of two components: kinetic pressure, P_{kin} , and thermal pressure, P_{th} . The momentum transferred to the substrate by the incoming flux of atoms (ions) determines the kinetic pressure. However, the kinetic

pressure is small in comparison to the thermal pressure, which depends on the average temperature of the substrate. The average temperature on the substrate surface generated by the impact of the ablated flow can be calculated through the maximum temperature on the target surface, T_{\max} , the laser repetition rate, and the pulse duration [73]. The thermal pressure and average temperature on the substrate were estimated as 20 kbar and 1600 K, respectively, for the 120-ns pulse laser and 40 kbar and 3000 K for the 60-ps laser by Gamaly et al. (1999, 2000) [31, 73]. These pressure and temperature values are close to the range of parameters most appropriate for the carbon-to-diamond phase transition to occur under equilibrium conditions.

One can see that an increase in laser intensity will increase the energy of the ablated ions and consequently will increase the temperature and pressure on the surface of the substrate, thus affecting the conditions for thin film formation.

4.1.2. Experiments: The Material Properties of the Films Produced

High average power, high repetition rate Nd:YAG lasers ($\lambda = 1.064 \mu\text{m}$) were used for laser ablation of carbonaceous targets and deposition experiments [73, 75]. Laser radiation with parameters of 60 ps, $3 \times 10^9 \text{ W/cm}^2$, and 76 MHz is absorbed well ($\sim 85\%$) by a graphite target and produces an almost fully ionized laser plume with a surface temperature (average over many pulses) in the range from 2500 to 3500 K [73]. Thin carbon film deposition was performed in a chamber evacuated to 10^{-7} Torr on a mica substrate. The surface morphology of carbon films with a thickness of 25–120 nm has been investigated with an atomic force microscope [73–75, 77]. Films with thicknesses of 20–25 nm appear to be almost atomically smooth with the surface root mean square (rms) roughness around 0.4–1 nm [73, 75]. The optical bandgap of 0.5–0.7 eV extracted from ellipsometry measurements and Raman spectra indicated that the deposited films had properties similar to the diamond-like amorphous carbon (a-C) films.

Studies of the influence of laser intensity in the range 10^{14} – 10^{16} W/cm^2 and wavelength in a range of 400–1000 nm on the properties of deposited films unveiled several interesting phenomena [73–76]. The energy distribution of ions which were ablated with short (around 100 fs), intense (in excess of 10^{14} W/cm^2), and prepulse free laser pulses has a pronounced two-bump form composed of a main thermal part, E_{th} , and a fast part, with energy 3–5 E_{th} [74]. Studies of the deposited films revealed that the transmission of the films increases with increasing laser intensity, while the ratio of sp^3 to sp^2 bonds decreases, being evidence of a less diamond-like character. The bandgap for these films determined with ellipsometry measurements was 0.85 eV, which supports the assumption of the amorphous nature of the films. Experiments using an intense short-pulse, high repetition rate laser demonstrated, along with atomic surface quality, an extremely high deposition rate up to a few micrometers/hour [73, 75], exceeding that for all other available methods of thin film deposition. It is instructive to compare with a deposition rate using a long pulse (~ 17 ns), low repetition rate (10–20 Hz) KrF laser (248 nm, 5–125 J/cm²),

where the deposition rate for the production of amorphous carbon films with high surface quality (rms roughness of 0.6 nm) constitutes 0.3–0.6 micrometers/hour [77].

4.2. Deposition of Complex Films

Laser ablation can be used to produce films of complex materials with the same stoichiometry as the original target. Provided that the laser intensity is chosen such that the bonds with the highest binding energy can be destroyed, laser ablation can produce an atomized beam containing the whole mix of constituent atoms. As a result, the laser plume contains a mixture of atoms with exactly the same atomic content and with the same atomic ratio as in an original target. Therefore the deposition process maintains the same stoichiometry in the deposited film or in a nanocluster as in the ablated target. As an example of complex structures being successfully deposited, we mention chalcogenide glasses (As_2S_3) [34] and high-temperature superconducting ceramics [78–80].

5. NANOCLOUDS PRODUCED THROUGH THE INTERACTION OF ABLATED VAPOR WITH NOBLE GAS

The ideal mode of formation for any nanostructure is bottom-up or atom-to-atom attachment in a proper place in space, and at the proper rate in time, in order to form clusters with desirable characteristics. To approach this mode, one should be able to control the formation process on a space scale of angstroms and on a time scale less than a picosecond.

An atomic beam for cluster formation can be created by laser ablation with short (picosecond and subpicosecond) successive laser pulses, with the repetition rate up to 100 MHz. In this case, the shortest controllable time scales are the laser pulse duration and a time gap between the pulses. The smallest controllable number of atoms is the number of atoms evaporated per single laser pulse. Of course, the decrease of a single pulse duration and increase of the repetition rate will lead to a smaller controllable time scale and number of particles per pulse. In principle, there is no upper (lower) limit: in the ultimate limit of extremely short pulses and the highest possible repetition rate, one has atom-by-atom evaporation with as short as necessary time control and consequently an atom-to-atom attachment process of cluster formation.

The process of nanocluster formation is composed of several stages, namely, the formation of a laser-produced flow of hot atomic vapors, plume propagation, diffusion, cooling/heating in a chamber, a cluster nucleation process, and a final stage of annealing, cooling, and stabilization. In what follows, we describe all the formation stages of individual clusters and compare with experimental data where available. We briefly discuss size-dependent cluster material properties and the internal structure of nanoclusters. We then discuss interactions with the substrate and the formation of cluster-assembled films.

5.1. Nucleation, Growth, and Annealing

It is instructive to consider the simplest case of the formation of clusters composed from one element. The most studied cases are those of carbon cluster and metal cluster formation. We consider, for example, the thoroughly studied carbon cluster formation process in a noble gas filling of the experimental chamber. There are also many studies of cluster formation in a reactive gas atmosphere [7–9, 81]. The processes of cluster formation in reactive gases are more complicated and less developed. Therefore, we restrict ourselves to interactions between atomic beams with noble gas. Many features of the formation process that we describe are common for the formation of clusters of different elements.

We should note that many essential details of cluster formation mechanisms have still not been uncovered, and some of the proposed mechanisms are questionable. There is no clear understanding or mutual agreement about the onset of the nucleation process, the progression toward cluster building, or growth termination. Many theoretical models have been proposed. But due to the lack of *in-situ* diagnostics, no experimental validation of the proposed mechanisms has been obtained to date. However, the general picture of cluster formation can be presented in a reasonable scenario. In the following we present a qualitative picture of cluster formation based on kinetic and thermodynamic arguments.

5.1.1. Nucleation and Growth

The cluster formation mechanism appears to be simple from first appearances. The hot vapor of ablated atoms rapidly expands in a cold gas. Thus, the thermodynamic approach of fast vapor condensation into minidroplets, that is, clusters, seems straightforward. Close examination, however, reveals that the process is too fast in comparison to the equilibration time. The vapor density is relatively low, and the atom-to-atom collision time is not negligibly small in comparison to the characteristic time of the process. Thus caution should be exercised in applying the thermodynamic approach for describing the cluster formation process. In the following, we discuss and compare the thermodynamic and kinetic descriptions of the cluster formation process.

Thermodynamic Approach—Condensation Nucleation is a process through which clusters of a new phase grow inside an initial phase, which has been heated above the phase transition temperature. In thermodynamics the nucleation process describes the early stages in phase transformation, such as condensation of gases during expansion or solidification of melts. The expanding vapor (plasma) of ablated atoms during interaction with a cold gas or substrate can be transformed into a supersaturated state. This state is thermodynamically unstable. Therefore, a vapor-liquid phase transition develops leading to the formation of nuclei of the new phase, minidroplets of liquid. If some fast annealing process can suddenly terminate further growth of these droplets, then nanoclusters can be formed.

The nuclei of the new phase are formed due to fluctuations in an unstable system. A nucleus can continue its growth only in cases where its radius exceeds a definite critical value. Classical condensation theory [82] predicts well the critical size of a nucleus when a liquid droplet forms,

starting the fast process of the phase transformation under the conditions of local thermodynamic equilibrium.

The small seeds (nuclei) of a new phase are created in the overheated, initially homogeneous, vapor phase due to fluctuations [82]. Such seeds are unstable structures because the formation of an interface between two phases is energetically unfavorable: to create a seed, the work to overcome the surface tension for the formation of a nucleus needs to be spent. The seeds with a size less than the critical value decay into the initial phase. The seeds with a size exceeding the minimum critical radius start to grow up, rapidly becoming the centers of the fast transformation into a new phase. The critical radius of a seed can be obtained from the condition of minimization of the free energy of a seed assuming that it has the form of a spherical droplet. Physically, this condition is equivalent to the balance between the surface tension and the thermal pressure. The critical radius of the seed is expressed through the temperature of the overheated phase, T , as [82]

$$r_{\text{cr}} = \frac{2\alpha}{P' - P} \approx \frac{2\alpha}{n_a(T - T_{\text{melt}})}$$

where α is the surface tension between the liquid and gas, P' is the transient pressure in a gas, and P is the pressure corresponding to the liquid-gas equilibrium: $P = n_a T_{\text{melt}}$. One can consider seed formation as the attachment of a single atom (or monomer) to the seed center, with a characteristic thermal velocity $v_{\text{th}} \sim (2T/M)^{1/2}$. This approach allows the estimation of the cluster size under conditions close to those in equilibrium. There have been numerous attempts to improve a classical theory of cluster formation by molecular beams under nonequilibrium conditions without considerable success. Review and discussion of these theories by Milani and Iannotta (1999) is available [3].

The critical radius is directly proportional to the surface tension between the liquid and gas phases and inversely proportional to the pressure of the expanding vapor. Therefore, as one can easily estimate from the above formula, the nanometer size clusters can be formed via the condensation process only in a very dense vapor with a density a few times, 3 to 10 times, lower than the solid density. It means that the formation of nanoclusters by vapor condensation from the supersaturated state might occur in a region very close to the ablated target. Note that the above description of minidroplet formation applies to a monoatomic homogeneous vapor in thermal equilibrium.

Let us now compare the above model to the experimental data of cluster formation. Hot silicon vapor was produced by laser ablation (ArF laser, $\lambda = 193$ nm, 15 ns, 1–3.9 J/cm²) of a monocrystalline silicon sample [83]. Silicon clusters with a diameter in the range of 1–4 nm were formed through interaction with a flow of pure helium (at pressure from 1 to 4 Torr). The silicon target was used as a substrate where the nanoclusters were collected. Patrone et al. and Marine et al. [83, 84] found that cluster size grows in direct proportion to the increase in laser fluence. However, the increase in laser fluence results in increases in the near surface temperature and pressure of vapors. Thus, in thermodynamics, it should result in a decrease in the critical radius of the nucleus of the new phase and therefore make easier the growth of large droplets. It was also demonstrated that the cluster size

decreases as the distance from the laser focal spot increases. The temperature at the substrate decreases as the distance from the focal spot increases. In accordance with the classical theory of expanding vapor condensation [66, 82], this must result in an increase in the number of critical nuclei for condensation, which is in contradiction to the experimental observation. The vapor condensation model has also been mentioned by Sattler [85], in relation to carbon nanotube formation, as a possibility for forming half-fullerene seeds for the further construction of nanotubes. One can note that condensation leads to the formation of a disordered (liquid) droplet. The complicated internal structure is a result of a microscopic atom-to-atom interaction. One can conclude that the direct application of the thermodynamic approach for explanation of the transient processes of nanocluster formation looks rather questionable. It allows an estimation of an approximate cluster size at best. Let's now consider the kinetic approach to the cluster building process.

Kinetics of Vapor–Gas Interaction The flow of atomic carbon is created by laser ablation near the surface of a target. The carbon cloud expands, carbon atoms collide with the filling gas atoms, exchanging energy, diffusing, and finally forming a mixture of carbon and filling gas with some average transient density and temperature. Thus, the conditions for the formation of clusters—“the primeval soup”—are created. The number density and temperature of this mixture change with the distance from the target. It is quite different near the target and near the substrate, several centimeters away. The processes of collision, diffusion, and atom-to-atom (atom-to-cluster, cluster-to-cluster) attachment can be described qualitatively on the basis of a simple kinetic theory [54, 86–87]. Depending on the masses of ablated atoms and the atoms of the filling gas, the processes of energy exchange will occur at different rates. If the masses of colliding atoms are comparable (for example, carbon flow with an argon fill), the carbon can lose a significant part of its energy even in a single collision. Hence, efficient energy equilibration occurs after several collisions: the carbon vapor is cooling down and the argon gas is heating up. The main processes which contribute to changes in the density of carbon atoms in the cluster formation zone are the following: delivery of atomic carbon by the target ablation, carbon losses due to diffusion out of the formation zone, and carbon consumption in the cluster formation process. On the basis of kinetic considerations, the scenario of carbon cluster formation in a carbon–argon mixture created by the high repetition laser has been suggested. We point out that the main features of this scenario are applicable to the cluster formation of any other element.

Kinetics: Nucleation by Monomer Addition Laser ablation creates an almost continuous inflow of hot carbon atoms and ions, with an average temperature of a few electron volts, into the experimental chamber. The shock wave generated by each pulse rapidly decelerates in the ambient gas atmosphere, and further propagation of hot atoms proceeds by diffusion. Initially the ambient gas is at room temperature (or the temperature of the furnace). The continuous inflow of hot carbons increases the partial density of carbons in the chamber, along with the temperature in the mixture.

When the carbon vapor temperature and the number density reach the level where the probability of carbon–carbon attachment becomes significant, the formation of carbonaceous clusters begins. The carbon consumption rate during this formation process significantly exceeds the evaporation rate due to laser ablation. Therefore, the carbon number density rapidly decreases to the value at which the formation process terminates. Thus, the ablation rate, target parameters, pressure, and properties of the ambient gas determine *the formation time* and, accordingly, *the size* of the cluster formed. Continuing laser evaporation leads again to an increase in the carbon number density to a value sufficient to resume the next cycle of cluster formation.

It has been suggested by Gemaly et al. [87] that the cluster formation process is composed of periodic stages of heating and cluster formation, with the time period depending on the initial argon density, the evaporation rate, and on the carbon attachment reaction rate, which in turn is a function of the temperature and density of the atomic carbon. It is clear that the average temperature of the ambient gas depends on the laser repetition rate. For example, in the case of a high repetition rate laser [73], during the short period of cluster formation (in comparison to the heating period), the argon gas does not cool down but maintains a temperature approximately equal to that required for cluster formation. As a result, the average temperature in a carbon–argon mixture appears to be high enough for formation of sp^2 and sp^3 bonds, as experimentally observed.

The maximum number of atoms in a cluster (or the maximum cluster size) from the kinetic viewpoint is directly related to the cluster formation time defined above. The characteristic time for N atomic cluster assembly in an argon–carbon mixture can be estimated under the assumption that the main building process is dominated by single atom attachment to a bigger cluster, taking the attachment cross section to be equal to the geometrical cross section for elastic collisions. This time is directly proportional to the ambient gas density and inversely proportional to the square of the partial density of single carbon atoms. These predictions qualitatively comply with the experimental data that small clusters (~ 6 nm, 10^4 atoms) are preferably formed at a low gas pressure of 1 Torr [37, 73], while carbon nanotubes (10^6 atoms) are formed at pressures of 300–500 Torr [27–30, 87]. Therefore, the kinetic approach can qualitatively predict the formation time and the size of the nanocluster. However, kinetic theory, as well as thermodynamics, fails to explain fundamental issues relevant to the internal structure of the nanoclusters and their unusual material properties already observed experimentally, for example, why clusters having a particular number of particles (magic numbers) are more abundant, which features of the formation process are responsible for the intricate structure of a cluster, and what are the reasons for the formation of crystalline or amorphous clusters.

5.1.2. Cluster Annealing and Stabilization

Laser ablation creates a dense homogeneous mixture of hot ablated atoms and atoms of an ambient gas that proved to be the most appropriate medium for the formation of three-dimensional clusters. The homogeneous mixture has high

symmetry—it is almost isotropic. Kinetics and thermodynamics theories can qualitatively explain why the hot atoms can form a cluster of a definite size, like an amorphous snowball, during the many “sticky” collisions. However, it is well known that nanoclusters have different and sometimes very complicated structures. A fundamental question then arises, namely, how does the transition from such a disordered gas phase to the highly symmetric molecule of fullerene [19], or a carbon nanotube [20, 21], or even the more complicated structural unit of carbon nanofoam [37] take place? The most natural answer may be found in the general theory of phase transitions for condensed matter, in the breaking of the initial high symmetry of a homogeneous gas and in the formation of primary seed structures displaying the specific symmetry obtained in the final structure.

Formation of a three-dimensional cluster breaks the initial high symmetry in the cluster formation zone. In the genesis of fullerene, C_{60} , for example, a lower symmetry cluster, pentagon or hexagon, displaying an axis of rotation of a higher order (5 and 6) is created. From the chemical point of view, the substance in the nanocluster formation zone is a random mixture of different low-dimensional carbon clusters (monomers, dimers, trimers, five- and six-membered rings, etc.) formed in the process of stochastic “sticky” collisions of carbon atoms in the carbon-ambient gas mixture. All of these clusters have a lifetime strongly dependent on the temperature. Generally, this lifetime increases with decreasing temperature. Simultaneously, the spatial amplitude of fluctuations decreases when the temperature falls to the critical temperature and below. The critical temperature is the characteristic temperature at which the particular structure begins to stabilize and becomes rigid [88]. The jump in the order parameter (a singularity), which manifests the appearance of a new symmetry, also occurs at this temperature. The free energy of a newly formed cluster at $T < T_c$ must include, in addition to thermal energy, the internal (strain) energy which is absent from a totally disordered state. The configuration entropy of a cluster also characterizes its particular structure. The minimization of the free energy determines the critical temperature for the defect-mediated phase transition from a disordered gas phase [89, 90] or, for the case considered here, the optimum temperature for nanocluster formation. This critical temperature, or rather optimum temperature for nanostructure formation, was found experimentally: for carbon nanotube formation this temperature is approximately 1200–2000 K [29, 40, 43]. For fullerene formation this temperature as seen in molecular dynamics simulations [91] lies in the range of 2000–3000 K.

The formation of three-dimensional carbon clusters can be understood in terms of a phase transition from a disordered to an ordered phase by the introduction of a specific defect assembly or seed with a new structure. In the case of fullerene formation, it is associated with the appearance of pentagon-shaped, or five-wedge, disclinations. This is similar to the conventional scenario seen for disorder–order transition phenomena in the growth of crystalline structures [88, 89]. The appearance of a disclination—a singularity in order parameter—in a hot mixture of unassociated carbon atoms echoes arguments presented by Anderson that “the fluctuations do become of quasi macroscopic size and

dimension at the critical point...” [88]. The defect in this context is a means for replacing the symmetry of an initial phase with that of a new one.

We should note that most of the studied three-dimensional carbon clusters display very complicated internal structure. For example, fullerenes and fullerene-like structures are embedded with pentagons, which are units relevant only to surfaces of positive curvature. It is likely that carbon clusters, which include surfaces with negative curvature where heptagons are the responsible topographic elements, have also been identified experimentally [37].

5.2. Electronic and Structural Properties of Individual Nanoclusters

Many properties, intrinsic properties of a particular bulk material, become dependent on the size of a system when the cluster size decreases to several nanometers. The thermodynamic and electrodynamic arguments which apply to the infinite system (when one can ignore boundary effects) become invalid for the description of the properties of very small particles.

The unique features of nanoclusters are directly related to their small size. That size lies between the atomic size and the macroscopic dimensions of many particles in a bulk structure. There are at least two main consequences for the physical and chemical properties resulting from size. First, a nanocluster is a system of many, but a limited, number of particles, say 10 – 10^4 , and behaves as a large atom with discrete energy levels. Second, accompanying a decrease in cluster size, the ratio of the surface to volume increases. In this case, the surface phenomena dominate the electronic and optical properties of a cluster. For example, in a cluster containing 1000 atoms, about a quarter of the atoms lie close to the surface, suggesting that these atoms may strongly influence the cluster properties.

5.2.1. Critical Cluster Size

It is for understanding the properties of nanoclusters to know at what cluster size (or at what number of atoms in a cluster) the material properties of an atomic system approach those of the bulk structure. Moreover, it is important to understand if all the material properties are changing at the same critical “threshold” size or if different properties change at different cluster sizes.

It was theoretically predicted [92] that small metal clusters ($n < 10$) would have a face-centered cubic (fcc) structure, while in bulk, the structure is body-centered cubic (bcc). It was observed later on [93] that a structural evolution from amorphous to fcc, and subsequently to bcc, structure occurs in W nanoclusters when the number of atoms in a cluster increases, in agreement with Oh et al. [92]. The critical cluster size for metallic chromium nanoclusters is determined to be 490 ± 100 atoms, and for Mo nanoclusters it is in the range of 1460–3900 atoms for the cluster–bulk transformation in a structural sense to be completed [94]. The surface-to-volume ratio is huge for small clusters and therefore the surface energy contribution dominates in the total cluster energy. The fcc structure is more compact than the bcc and thus provides a lower surface energy and overall lower total

energy of a cluster. As will be shown in the next section, the critical cluster size appears to be different for different materials and for different properties.

5.2.2. Size Effects

Quantum Size Effects A system of particles in a finite volume has discrete energy levels. In general, the distances between energy levels, in general, decrease exponentially with increases in the number of particles. In bulk, the interference of electronic wave functions results in a band structure. However, at the opposite limit, when the size of the system decreases to the nanometer scale, the energy bands split again into energy levels. For example, the difference in energy between the electronic levels, $\Delta\epsilon$, in a small metal cluster increases in inverse proportion to the size of the cluster, R , as $\Delta\epsilon \sim v_F/R$, where v_F is electron Fermi velocity [95]. If the applied electric field $eER \ll \Delta\epsilon$, and the frequency of the external field complies with condition $\omega \ll v_F/R$, then the small metallic particle behaves in such a field like an atom with a certain polarizability. A moderately small cluster possesses a larger polarizability than that following from the classical polarization of a metal sphere.

Size-dependent photoluminescence of silicon nanoclusters has been observed experimentally where the cluster size ranged from 1 to 3.5 nm [83, 84]. Analysis of the internal structure of the silicon clusters using high-resolution transmission electron microscopy (HRTEM) revealed that clusters had a crystalline structure and nearly spherical shape [84]. When the cluster sizes were decreased from 3.5 to 1 nm, the peak in the luminescence spectrum shifted from 750 to 300 nm.

Neutral silicon clusters ranging in diameter from 1 to 20 nm were produced by laser ablation of a silicon target in an ambient atmosphere of helium at a pressure of 8 Torr and extracted into a vacuum as a cluster beam. The cluster beam was then scattered by an argon beam flowing in a direction perpendicular to the cluster beam. Clusters of different sizes were deposited onto substrates positioned at different distances from the axis of the cluster beam. On the substrate placed directly on the beam axis, spherical isolated clusters with a mean diameter of 10 nm were deposited. The average size of the clusters decreases as the distance from the axis of the cluster beam increased.

The nanocluster films exhibit a strong red photoluminescence after being exposed to air. The energy of the photoluminescence peak changes between 1.42 eV (845 nm) and 1.72 eV (700 nm) depending on the substrate position: the farther from the cluster beam axis, the higher the energy. Wu et al. [96] relate the observed energy shift to the quantum confinement of carriers in surface-oxidized silicon nanocrystals. A blue shift in the energy of the photoluminescence peak, of up to 2.1 eV, in surface-oxidized porous silicon quantum dots was also observed by another research group when the size of the dot decreased from 3 to 2 nm [97].

These observations qualitatively comply with the effect of increasing the distance between the energy levels while the cluster size decreases. Note that such a luminescence has not been observed in bulk silicon.

Formation Energy It was experimentally determined that the energy for the formation of individual clusters depends on their size and shape. Tin nanoclusters containing from 95 to 975 atoms were formed by laser ablation of tin in a helium atmosphere [98]. For one type of tin clusters it was found that the formation energy was proportional to $(1.64 \pm 0.04 \text{ eV}) \times N^{-1/3}$, indicating compact spherical-like shapes. Another class of clusters had almost constant formation energy of $0.4 \pm 0.05 \text{ eV}$. The theory developed for elongated neutral silicon clusters indicates [99, 100] that the surface-to-volume ratio of in these clusters is constant, which indicates that the formation energy was independent of size. It was suggested that the second type of cluster has a quasi-one-dimensional geometry. Thus, in the first type of cluster, the surface energy changes with the change in the number of atoms in the cluster, while in the second cluster type, the contribution of the surface energy to the total cluster energy is the same for clusters of different sizes. The experiments [98] clearly demonstrate the strong influence of surface energy on the formation energy of a cluster: the smaller the cluster is, the easier it is to form.

Melting Temperature: Solid-like to Liquid-like State Transition It has been demonstrated both experimentally and theoretically that the melting temperature of nanoparticles and nanorods is significantly lower than that for the bulk material (see, for example Wang et al., 2002 [101] and references therein). The melting point of platinum nanowire was found to be 400 °C [102] (the bulk value 1772 °C), while the melting temperature of 4.6-nm-thick palladium was 300 °C, which is drastically lower than the bulk value of 1552 °C [103]. Through molecular dynamic simulations [101], the melting temperature of gold helical cylindrical nanowires was found to be $\sim 1100 \text{ K}$, that is, lower than the bulk value of 1357 K, but higher than that of gold nanoclusters.

Usually equilibrium melting starts from the surface and then propagates into the interior. Surface atoms have the fewer nearest neighbors and weaker binding, which may lead to a lower melting temperature at the surface than that for the bulk. Large surface-to-volume ratios and quantum size effects are the two major factors believed to be responsible for this dramatic decrease in the melting temperature of nanoclusters compared to the bulk value.

In contrast, it was found that the interior melting temperature in gold nanorods appeared to be higher than that of the atoms on the surface. Melting starts from the interior atoms, while surface melting occurs at relatively high temperature. This unique thermodynamic behavior, compared to the above description, is closely related to the helical structure of the nanorod. In this case, surface melting is responsible for the overall melting of the structure, and the effect of higher interior melting temperature entirely relates to the complicated internal structure of a rod [101].

The transition from a solid-like to a liquid-like state for finite systems, where the surface and boundary effects are dominant, is not as well defined as that for a bulk solid. The transition may exhibit the intermediate state of the coexistence of different structural phases (isomers) of the same cluster [104]. The solid-liquid phase transition in a system with a finite number of particles is described in terms

of a potential energy surface [105]. Stable clusters correspond to minima on the potential energy surface. If a cluster acquires sufficient energy, the transition from one isomeric form of a cluster to another corresponds to a “jump” over the saddle-like potential barrier separating the minima. The more liquid-like a cluster becomes (the higher the temperature and internal energy), the shorter the time for a transition from one isomeric form to another. One can define the transient state as a state when the lifetimes for the different isomeric forms of a particular cluster become comparable [104].

The lifetime of cesium halide clusters with different spatial arrangements of constituent atoms were observed using temperature-dependent photoelectron spectra and applying the pump-probe technique [104]. The clusters were produced in a laser vaporization source. A plume of laser-ablated cesium halide vapor was swept through a temperature-controlled nozzle by a flow of helium. The clusters were formed through helium-vapor interaction and then mass selected using time-of-flight mass spectrometry. The anions of desired mass were directed into a magnetic bottle, where the electrons were then detached by the action of 1- to 2-ps-long probe laser pulses, and the electron spectra were measured. Three different isomers of cesium halide consisting of four cesium atoms and three iodine atoms were identified: cube, flat ladder, and ring. The transition between these structures proceeds in the following succession: cube \rightarrow ladder \rightarrow ring. At a temperature ~ 500 K, the lifetime for all three isomers become of the same order of magnitude of several tens of picoseconds. Therefore this temperature can be considered the cluster melting temperature: at this temperature all three isomers are continuously transforming to each other, thus making any particular structure indistinguishable, as in a liquid drop. From the measurements, the time for this phase transition to occur was estimated to be in the range of ~ 100 ps. One may note that the melting temperature for the bulk cesium halide is 900 K.

Adsorption Energy Two other important microscopic parameters, which depend on the cluster size, are the adsorption energy and the bond distance of single atoms on surfaces. The adsorption energy, or energy of an interaction of an ad-atom and the surface, increases as the number of atoms decreases. Conversely, when the number of atoms in a system increases, this energy converges to the final constant value corresponding to the bulk solid [106]. For example, the adsorption energy for a copper atom on a four-atom copper cluster comprises 3.6 eV, whereas the adsorption energy saturates at 2.7 eV for clusters with a number of atoms larger than 56 [106].

5.2.3. Dielectric Function for a Single Metal Cluster

The qualitative dependence of the dielectric function of a single metal cluster on its size can be understood on the basis of simple arguments of general physics. Let us assume that the dielectric function for the metal cluster in an external electric field with frequency ω has the same form as the

function for a conventional metal, for example, having the Drude form [63]:

$$\varepsilon = 1 - \frac{\omega_{pe}^2}{\omega(\omega + i\nu_{eff})}$$

here $\omega_{pe} = (4\pi e^2 n_e / m_e)^{1/2}$ is the characteristic electron plasma frequency, n_e , m_e are the electron number density and electron mass, respectively, and ν_{eff} is the effective frequency of collision between electrons with the lattice, which is responsible for the energy dissipation. We assume that the cluster of radius R contains N atoms of a metal with one conductivity electron per atom. One can reasonably suggest that all conductivity electrons fill the whole volume of the cluster homogeneously like a jellium [2, 107, 108]. The electron number density can be expressed as $n_e = Ne/(4/3\pi R^3)$, thus giving the dependence of the plasma frequency on the cluster size.

One can see that the energy dissipation of an external electric field imposed on a small cluster also depends on the size of the cluster. Indeed, in a nanometer size metallic sphere, the mean free path of an electron between collisions significantly exceeds the cluster diameter $l_{mfp} \gg R$. Therefore, the electron can lose its energy only in collisions with the cluster walls. The characteristic frequency of this process is proportional to ν_F/R . Hence, the effective frequency of energy dissipation is $\nu_{eff} \sim A\nu_F/R$, where A is a dimensionless proportionality coefficient. It was shown that the classically derived $(1/R)$ law also follows from quantum mechanical calculations (see the thorough discussion of this problem and references by Krebig and Vollmer (1995) [107]). It appears that this law represents a fundamental quantum size effect; it also reflects the surface-to-volume ratio. These simple relations show how the optical properties of metal nanoclusters can be controlled by their size, which suggests many applications. We should note that the dielectric function of a single isolated cluster has not yet been determined experimentally.

5.2.4. Static Polarizability of a Single Metal Cluster

From the viewpoint of classical electrodynamics [63], a metal sphere in an external static electric field E acquires an induced dipole moment $P = R^3 E$, which is proportional to the volume of the sphere. However, close consideration of the dipole moment even in frames of a simple jellium model shows that electrons are spilled out of the cluster boundary (defined as $R \sim N^{1/3}$) at a distance δ , depending on the nature of the metal. Usually, this distance is $\delta \sim 1.3$ – 1.5 Å. Thus, the nanocluster dipole moment is expressed as $P = (R + \delta)^3 E$. These estimations, in the frame of a simple jellium model, are well supported by quantum mechanical calculations [107]. The important conclusion follows that the small metal sphere possesses a polarizability larger than that predicted by classical electrodynamics due to the effective increase in the cluster radius caused by spilling out the electric charge. The change in polarization can be controlled by the size of the particle. This effect was observed experimentally [2] with reasonably good agreement with the theory.

5.2.5. Shell Model for a Simple Metal Cluster

The abundance mass spectra of alkali metal clusters produced and detected by Brack (1993) [108] revealed a striking feature: clusters with a particular mass value, containing a specific number of atoms—“magic numbers”—appeared to be much more abundant in comparison to the average mass of the clusters produced. It is established now that this characteristic abundance pattern holds up even for clusters containing several thousand atoms [2, 108]. It was recognized that the abundance pattern reflects the electronic structure of the cluster and is indicative of the most stable clusters. Clusters of metal atoms are considered a unified edifice having a common electronic structure, with all valence electrons belonging to all constituent atoms and filling corresponding shells that are characterized by specific quantum numbers for such an edifice as a whole. Therefore, maxima in the mass abundance spectra have been identified as clusters with closed electronic shells. Just as for atoms, the electronic system of a cluster with exactly the right number of electrons to complete a shell is very stable. If one more atom is added to a cluster with a closed shell, the valence electrons of this extra atom will occupy the higher energy state, and hence the stability of the new cluster is reduced. The reduced stability is reflected in reduced abundance, which explains the experimentally observed drops in the cluster abundance spectra after each shell-closing number [2]. The theory also predicts that closed-shell clusters have a spherical shape, while open-shell clusters are significantly distorted. Molecular dynamics and quantum chemical calculations later supported the initial simple theories, revealing fundamental physical features of the shell model. The theory of the cluster shell model is now well developed, with many predictions experimentally confirmed (for comprehensive review, see de Heer (1993) and Brack (1993) [2, 108] and references therein). While it is difficult to determine the cluster size and shape experimentally, through measurements of the optical properties of the clusters it is possible to make some conclusions about the influence of shape on the properties of the clusters.

5.2.6. The Affinity between the Internal Structure, Material Properties, and Formation Conditions of Nanoclusters

The discovery and studies of new nanostructured carbon phases, such as fullerenes [19, 51] and nanotubes [20, 21, 56], has opened a new era in materials science. It has been discovered that minute changes in the spatial arrangement of carbon atoms in the space scale of tens of angstroms can profoundly change the electronic properties of these systems from a semiconductor to a metal [110, 111], from a conductor to a superconductor [112, 113], and even from diamagnetic to ferromagnetic [114], with a drastic difference from the bulk properties of graphite, diamond, or amorphous carbon. One could expect that structural rearrangements at the nanometer scale might also change the properties of other materials in ways similar to those with the carbonaceous structures. To date thorough studies have been performed with carbon nanoclusters. Below we concentrate on structural and material properties in connection with the relevant

formation conditions of carbonaceous clusters and clustered films.

Laser ablation was used to generate carbonaceous nanoclusters under different experimental conditions: in the ambient gas at different pressures; with additional gas heating; and with different catalysts. A broad variety of different nanostructures have been created which now form the family of “fullerenes.” This family includes single-shell fullerenes, C_{60} and C_n [19], multiwalled hollow nanoparticles (fullerene onions), single-wall and multishell carbon nanotubes [20, 21, 29, 56], hypothetical carbonaceous structures with negative curvature [115–118], carbon nanohorns [119], and carbon nanocones [120]. Both the nanocluster formation energy and kinetic factors define the formation conditions and therefore the abundance of the particular nanocluster [118, 121]. The primary product of the interaction between the laser-produced plume and a noble gas is a complicated network of different nanostructures mixed together and interconnected. In order to study the individual nanotubes the meticulous processes of separation and purification of the primary material are used [21]. Another method of cluster selection and separation is to preionize the clusters using a special short-wavelength laser and then to selectively remove clusters with an applied electric field [2, 3, 45, 122].

Cage-like Structures A plume of carbon atoms and ions ejected during the laser ablation of a graphite target was made to interact with a noble gas buffer [45, 122]. Carbon clusters created in such an interaction were then detected by a mass spectrometer. The measured abundance spectra may be regarded as an accumulated “snapshot” of salient features in the nucleation and growth of carbon clusters in a time sequence. A typical mass spectrum of positively charged clusters is bimodal [45, 122]. The peaks in the mass abundance spectra correspond to clusters of enhanced stability. The maximum in the first group of clusters ($n < 30$) corresponds to clusters comprising 11 carbon atoms, while the maximum in the second group ($30 < n < 100$) relates to the famous fullerene, C_{60} , molecule consisting of 60 carbons [19, 122]. Any closed-shell-like exclusively carbon cage is referred to as a fullerene [123]. The fullerenes are viewed as graphitic sheets distorted by inclusions of topological defects, such as five-membered rings, or pentagons. The simplest ball is a pentagonal dodecahedron comprising 20 carbons. The appearance of a pentagon is the signature of a curved surface with positive Gaussian curvature. C_{60} , which is the most stable, and central to the fullerene family, consists of 12 pentagons and 20 hexagons.

The range of clusters is composed of one- and two-dimensional structures (linear and ring clusters, $n = 3$ –20) along with three-dimensional clusters, like the closed cage of the fullerene molecule. Multiwalled hollow nanoparticles (nested fullerenes or onions) can be also formed under similar conditions [123]. All these clusters are formed in an almost homogeneous mixture of carbon and noble gas atoms at pressures of several hundred Torr and temperatures of 1000–2000 K. The estimates of the scale of the temperature for fullerene formation may be made from the self-energies of nanoclusters [118, 121]. The additional energy that it is necessary to spend for fullerene formation, in comparison

to the flat graphite sheet, ranges from 0.6 to 0.4 eV/atom [118, 121]. This means that the optimum temperature for the formation of such clusters can be in a range of several thousand degrees Kelvin. This estimate qualitatively complies with the experimental measurements.

The relative population of a particular cluster is governed by cluster growth kinetics. In turn these kinetics depend on the transient partial number density of carbon atoms in the carbon–noble gas mixture and the transient temperature in the cluster formation zone. Therefore, one can conclude that under isotropic conditions, no cluster of preferential symmetry can be formed but only the simple clusters, or clusters with a high symmetry of the order 5 and 6, like fullerenes.

Carbon Nanotubes Another carbon nanocluster, the nanotube, is also produced by laser ablation at high pressure in an almost homogeneous mixture of carbon atoms, noble gas atoms, and a metal catalyst at a temperature of around 1000–2000 K. The required optimal ambient gas pressure was found to be around 500 Torr for the formation of carbon nanotubes, while at 100 Torr the efficiency of carbon nanotube formation was drastically reduced. Carbon nanotube can be imagined as a graphitic sheet rolled up and stitched without seams. Therefore, nanotubes consist entirely of six-fold rings, hexagons. The straight nanotube possesses an axial symmetry, which is apparently absent in the zone of formation. However, it was observed that carbon nanotubes formed in a homogeneous carbon–noble gas mixture were only formed in the presence of metal catalysts at a concentration of ~1% of the total carbon content. These catalysts are usually transitional metals, such as cobalt, iron, or nickel or a mixture of them. Thus, there is strong experimental evidence that a catalyst is responsible for the formation of axially symmetric structures. It may be that catalytic particles are either atoms or metallic clusters containing many atoms; however, there is no thorough theoretical explanation of catalyst action in the formation process.

Nanotubes in general are helical, meaning that the tube is twisted around its axis. In the spirit of defects and energy arguments, one can assume that tubules grow helically with the introduction of a screw dislocation, as metal “whiskers” grow [113]. The theory shows [110, 111] that a chiral tube can be generated in such a way that no distortion of bond angles is introduced. This distortion relates only to the cylindrical curvature of a tube. Helicity is responsible for one of the most striking properties of nanotubes. Depending on chirality one third of the tubules will be metallic and two thirds semiconducting. The existence of metallic and semiconductor nanotubes has been observed experimentally [124]. Raito et al. [111] have suggested that a large fraction of metallic tubules might be formed if the initial seed for the tube cap is centered around a pentagon. However, the proper conditions for the preferential formation of such seeds needs to be formulated. These properties imply many important applications in the future. For example, one can imagine nanometric conducting wires, microscopic metal–semiconductor devices for nanoelectronics or photonics, and many other possibilities. Nanotubes also possess extraordinary strength, with the highest Young modulus of all known materials. This was deduced from the observation of temperature vibrations of freestanding tubes in a transmission electron microscope [125].

It follows from molecular dynamics calculations and a simple elasticity approach [118, 121] that the energy necessary for the formation of tubes consists entirely of the energy required to bend a graphite sheet into a tube, which is ~0.2 eV per carbon atom. Comparison to the fullerene self-energy implies that the tubes are more stable than fullerenes. Another conclusion is that the temperature required for nanotube formation may be somewhat lower than that for the creation of fullerenes and may be around 2000 K, which qualitatively complies with the experimental data presented in Section 2.

Structural Units of Carbon Nanofoam According to theoretical predictions [115–118], hypothetical carbonaceous structures with negative, or hyperbolic, Gaussian curvature, branded “schwarzite,” are more complex than fullerenes (elliptic curvature) and buckytubes (parabolic curvature). Sevenfold rings (heptagons) are the topological elements (disclinations) responsible for the generation of schwarzite structures. The exact shape of a single negative disclination is not yet known; however, calculations show that heptagons, in terms of local structure, are energetically less costly (more stable) than pentagons, with the self-energy per carbon in a range of 0.1–0.15 eV/atom [118, 121]. This also means that the temperature conditions for hyperbolic structure formation may be close to those for carbon nanotubes. It has been suggested that the complicated spatial structure of schwarzites might result in unusual electronic properties.

Recently, low-density cluster-assembled carbon nanofoam was produced by laser ablation of glassy carbon in an argon-filled chamber at a pressure range of 0.3–1 Torr [37, 114]. Diffusion-limited aggregation of carbons in the carbon–argon mixture and the subsequent fast quench resulted in a unique, fractal, all-carbon foam deposited on a substrate. Preliminary studies revealed the presence of a hyperbolic schwarzite structure, rather than the expected nanotube-like structures. The foam structure was characterized by scanning electron microscopy, transmission electron microscopy, HRTEM, small-angle X-ray scattering, Raman spectroscopy, EELS, Rutherford backscattering, and surface-area measurements [37, 54, 114]. These studies revealed that the foam is made of a web-like fractal network of randomly interconnected clusters, 6–9 nm in diameter, as can be seen in Figure 8. HRTEM images demonstrated that individual clusters possess an internal periodic structure with a period of ~5.6 Å. The spatial variation of sp^2/sp^3 bonding across a single cluster was mapped using a PEELS with a spatial resolution of 1 nm [37]. These results indicate that sp^2 -bonded carbons prevail in the core region of clusters, whereas sp^3 -bonded carbons dominate near the cluster boundary. The measured high dc resistivity of the foam suggest that these sp^3 -bonded carbon atoms are responsible for sticking the clusters together.

The most salient property of the foam is its unusual magnetic behavior. The freshly produced foam is strongly attracted to a permanent magnet, just like a metallic dust, which demonstrates the existence of an intrinsic positive magnetic moment. Only the structural rearrangement of carbon atoms in the foam can be a reason for the dramatic change in the magnetic properties of this all-carbon system. Electron spin resonance measurements gave the density

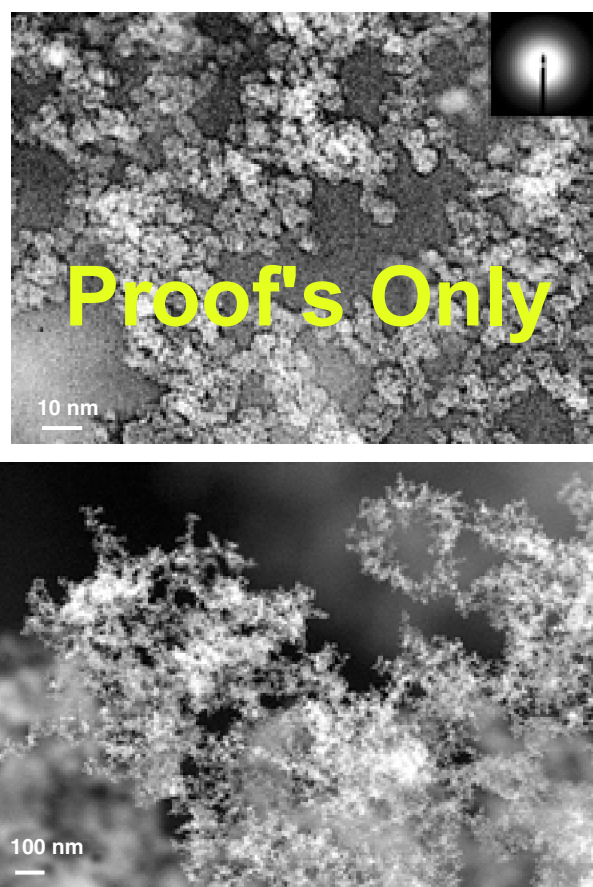


Figure 8. Transmission electron micrograph of carbon nanofoam (left) showing that the foam is assembled from 6-nm clusters. The SEM image (right) shows the web-like structure at lower magnification.

of unpaired spins up to 1.5×10^{20} spins per gram, or one unpaired spin per several hundred carbon atoms.

The ferromagnetic behavior exhibited by the new phase of carbon is extremely unusual in comparison to all known allotropes of carbon. Graphite, diamond, fullerenes, multiwalled carbon nanotubes, and single-walled carbon nanohorns possess a diamagnetic susceptibility in the range of -10^{-5} – -10^{-6} emu/g. It seems natural to suggest that the observed ferromagnetic behavior can be traced to the complex microstructure of the foam.

The origin of magnetism in cluster-assembled carbon foam has been theoretically studied using a geometry which contains hyperbolic, negatively curved surfaces [114]. The basic structural unit is a tetrapod that exhibits many of the structural features observed in experiments. The core structure consists of warped sp^2 -bonded carbon segments terminated by sp^3 carbon atoms at the hydrogen-passivated edges of the four extremities. In a tetrapod, like in other schwarzite-related structures, tubular segments of 0 Gaussian curvature coexist with convex segments of hyperbolic, saddle-like regions of negative Gaussian curvature. The radius of curvature in this basic unit is close to 6 Å, which is consistent with the superstructure found in the diffraction pattern. The tetrapod-like building blocks can be assembled into a rigid foam structure with a very low density that compares to the measured density of 2–20 $\mu\text{g}/\text{cm}^3$. The threefold

coordinated carbon atoms in the sp^2 regions form a network of hexagons and heptagons only. These trivalent carbons are sterically protected within the system of single and double bonds imposed by the sp^3 -terminated tetrapod and occur in groups of three. The number of unpaired spins was found to be robust with respect to size and boundary shape variations within the tetrapod. However, this number depends sensitively on the bonding topology in the regions of the negative Gaussian curvature. Subclusters (tetrapods) containing 264 and 336 carbon atoms have been considered, and the predicted magnetic moment in a C_{264} tetrapod agrees well with the experimental observation.

Stabilization of carbon radicals by steric protection has been known since the synthesis of triphenylmethyl by Gomberg in 1900 [126]. This is the first time to our knowledge that trivalent carbon radicals embedded into hyperbolic surfaces have been identified in an undoped all-carbon nanocluster prepared under specific conditions by laser ablation.

The ferromagnetism found in these complex nanoclusters occurs as a consequence of nanometer-sized conducting segments containing atoms with different electronic configurations. It appears that a careful preparation of conditions for nanocluster formation by laser ablation may lead to similar changes in the structural and electronic properties of different materials.

Fractal Nanoclusters Nucleation of a new phase is one of the processes where the fractal nature of the object often manifests itself. The generally accepted models for cluster growth include diffusion-limited aggregation, cluster-cluster assembling, homogeneous nucleation by monomer addition, and others. All the models assume that the nucleus, the seed of the new phase, has a spherical shape on which the further assembling of the structure occurs. Experimental evidence has been presented by Zenkevich et al. [127] which shows that gold clusters of ~ 5 nm in diameter have a fractal structure with fractal dimension of $D = 1.33 \pm 0.08$. These clusters were deposited on the surface of highly oriented pyrolytic graphite by laser ablation using an Nd:YAG laser with the following parameters of ablation: $\lambda = 1.06 \mu\text{m}$; 15-ns pulse duration; 25-Hz repetition rate; average intensity $\sim 10^9$ W/cm. The authors [127] suggested that the shape and dimension of the clusters are determined by the rate at which atoms arrive at the surface where the formation occurs and by the symmetry of this surface. It was proposed that the formation of clusters proceeds under highly nonequilibrium conditions by the attachment of an ad-atom to the fractal nucleus.

6. CLUSTER-ASSEMBLED MATERIALS

With the laser technology that is currently available, it is possible to ablate any existing material—refractory metals, complex composites, and dielectrics—if the laser parameters are chosen according to the properties of the material. The proper choice of laser parameters and conditions in the experimental chamber (pressure of the ambient gas or vacuum) defines the mass distribution in a cluster flow. The size of the clusters produced ranges from several atoms to tens of thousands of atoms per cluster. Clusters then can be deposited on a substrate to form a cluster-assembled film [3].

Films of clusters embedded in various codeposited matrices have been produced [128]. Very often such a film possesses material properties drastically different from those in the bulk of the initial material.

Cluster networks can be classified into two categories [5]. The first one comprises clusters embedded in a host matrix and well separated from each other. The properties of such structures depend on the properties of the individual clusters and that of the host matrix. The dielectric properties of the cluster-embedded composites depend on low and easy-to-change filling factors (~ 0.01 vol fraction of clusters) and on cluster-to-cluster contacts and connections. The second category includes cluster networks—sponge, froth, or foam-like structures—with properties which are drastically different from those of isolated clusters and which strongly depend on intercluster connections and interactions.

6.1. Cluster-Assembled Films

The flow of nanoclusters hits a substrate and starts building a deposit. First of all we shall distinguish between cases when the cluster-assembled film grows on a substrate in a vacuum [3, 32, 33] and in a noble gas-filled chamber [37, 83, 84, 114].

Molecular dynamics simulations of film growth by energetic cluster impact in a vacuum have shown the influence of cluster energy on the morphology of the film [129]. It is now widely accepted that the energy of a cluster must be sufficiently low in order to prevent the splitting of a cluster during cluster–substrate impact. The straightforward idea of “random paving” on a substrate seems to be in contradiction to experiments: it appears that film morphology depends on the cluster size [128]. Indeed, gold, antimony, and silver clusters, comprising 250–300 atoms, 2 nm in diameter, form large branched and well-separated islands with definite long-range order when deposited on a graphite surface.

The presence of an evaporation cell in the deposition chamber allows the production of films with clusters embedded into different matrices. Harbich et al. [130, 131] produced films of mass-selected metal clusters (Ag_n and Au_n) embedded in various solid matrices of Ar and Kr using this technique.

Gold clusters, comprising 250–300 atoms, embedded in various matrices (SiO_x , LiF, and MgF_2) are randomly distributed over a film surface. It was demonstrated that the cluster volume fraction of Au clusters embedded into a SiO_x matrix can be easily changed from 2 to 11% [128]. Therefore, films with variable dielectric function can be produced for a range of optical applications.

Another interesting application relates to the deposition of transitional metal clusters onto different substrates to produce magnetic films for high-density memory devices and spin electronics. Films with the size-controlled clusters of iron, cobalt, and nickel have recently been produced [128]. The incident free cluster size distributions were centered on Fe_{150} , Co_{300} , and Ni_{300} . Cluster-assembled films with thicknesses up to 100 nm were produced. These films have a granular structure with a grain size of 3–5 nm, slightly larger than the size of the incident cluster size resulting from the diffusion and coalescence of clusters.

Cluster-assembled films about 100 nm thick were produced with carbon cluster beams. The mass distribution in

the beams was centered on C_{20} , C_{60} , and C_{900} . These films have a highly porous nanostructured morphology resulting from a random stacking of incident clusters. The density of the films is in the range of 1 g/cm^3 , which is much lower than that of conventional carbonaceous structures. The most interesting structure appears to be C_{20} “amorphous” film with a short-range order of 15 nm, with pure sp^3 hybridization and the absence of any long-range order.

Similar films were produced with silicon cluster beams with the size distribution centered on Si_{50} . It is suggested that the presence of a large number of pentagons may significantly change the electronic structure of the clusters. These silicon films also have a granular structure and they are highly porous. The most unusual feature of these films is a strong visible luminescence at $\sim 750 \text{ nm}$ comparable to that seen in porous silicon and recently observed in 3.5-nm silicon clusters [83, 84].

6.2. Magnetic Properties of Cluster-Aggregated Films

Monodispersed cobalt nanoclusters, with cluster sizes varying from 300 to 9000 atoms, were produced by the cluster-beam technique [132]. These clusters were embedded in Cu and SiO_2 substrates, where the cobalt volume concentration varied from 10 to 50%. The magnetization of cobalt in such structures is always lower than the bulk value. This magnetization increases with increasing cluster size and decreases with increasing Co concentration for a given cluster size. Calculations of intercluster exchange interactions are used to qualitatively explain the magnetization data as a function of Co concentration in good agreement with the experimental results [132].

6.3. Nonlinear Optical Properties of Nanoclustered Films

It was found [133] that Si films deposited by laser ablation exhibit a nonlinear refractive index change, as high as $\Delta n = -0.5$ at a wavelength of $\lambda = 532 \text{ nm}$ for films with an average thickness of 200 nm. These films consist of large droplets composed of crystallites with hexagonal wurtzite symmetry and with nanoclusters interspersed between them. The crystallographic symmetry of these droplets was observed with Raman spectroscopy, as well as linear and nonlinear optical measurements, when the films were annealed under various conditions. The authors attribute the large nonlinear refraction coefficient to the hexagonal wurtzite symmetry of the crystallites, which raises the possibility of developing very efficient nonlinear optical devices [133]. However, the origin of this nonlinearity is not fully understood.

6.4. Electrical Conductivity of Nanoclusters and Cluster-Assembled Materials: Quantum Charge Transport and Localization

Another interesting property of the nanocluster-assembled system relates to electrical conductivity. It appears that the “conductivity quantum,” or conductivity scale of $2e^2/h$, plays

an important role in the electric conductance through the “bottle necks” connecting the nanoclusters in the cluster-assembled systems. Simple scaling illustrates the appearance of the “conductivity quantum” or “resistance quantum,” h/e^2 , when one considers the charge transport at the atomic space and time scales. The motion of electrons with charge e , mass m , and number density n in an applied electric field E of high-frequency ω generates the current density

$$j = env \approx \frac{e^2 n}{m(v + i\omega)} E \equiv \sigma E$$

This is Ohm’s law, where v stands for the electron collision frequency responsible for the energy dissipation (or resistance $1/\sigma$). The full current, $I = jS$, flowing through the sample with a cross section S , and length L , and containing a total number of electrons $N = nSL$, can be presented in the form

$$I \approx \frac{e^2 N}{mvL} E \approx \frac{e^2 N}{mvL^2} V$$

We assume $\omega \ll v$, which always holds for metals, and $E \propto V/L$ (where V is a potential). The resistance R , can be expressed as

$$R \approx \frac{NV}{I} = \frac{mvL^2}{e^2}$$

Considering all parameters at atomic scales, that is, taking the collision frequency as the same order of magnitude as the atomic frequency, $v \cong e^2/a_B$, and $L \cong a_B$, where $a_B = \hbar^2/me^2$ is the Bohr radius, one obtains the quantum unit of resistance as

$$R_0 \approx \frac{\hbar}{e^2}$$

This unit comprises 2.5812×10^4 ohm. Most probably this value of conductance (resistance) separates two different regimes of high and poor conductivity, giving the percolation and localization regimes [134].

The conductivity in nanowires of atomic dimension behaves in the jump-like manner of quantum charge transport. The electrical conductivity of small silicon clusters ($n = 1-10, 13, 20$) placed between atomistic aluminium and gold leads has been investigated using the *ab initio* nonequilibrium Green’s function formalism [135]. All clusters display metallic conductance ranging between one and two quantum units, $2e^2/h$. The transport properties of these cluster junctions may be understood in terms of both the band structure of electrodes and the electronic states of the cluster, modified by the lead environment and size effects. The resistance in this system is $R \sim R_0$.

Carbon nanofoam composed from well-defined carbon clusters of 6–9 nm in diameter, randomly interconnected in a web-like fractal structure, demonstrates a different limit case for conductivity [49]. The resistivity of the as-deposited foam, measured in the voltage range ± 100 V, demonstrates nonlinear current–voltage characteristics with strong hysteresis. The resistivity of the foam after annealing is equal to $1-3 \times 10^9 \Omega/\text{cm}$ at room temperature and $1-10 \times 10^{13} \Omega/\text{cm}$ at 80 K, which is similar to that of amorphous diamond-like films. Thus, resistance of the foam exceeds R_0 by many

orders of magnitude. One can assume that the electrons in a foam are strongly localized in nanoclusters, and the electron conductivity has a tunneling character.

6.5. Photoluminescence in GaAs Nanoaggregates

Laser ablation of a single crystal GaAs target in a vacuum or Ar gas has produced nanoclusters of GaAs [136]. Atomic force and transmission electron microscopy have shown that most of the clusters were spherical, with diameters in the range of 1 to 50 nm, with a peak size distribution between 5 and 9 nm, depending on the Ar gas pressure or laser fluence. X-ray diffraction, solid state nuclear magnetic resonance, Auger electron spectroscopy, electron energy-loss spectroscopy, and high-resolution transmission electron microscopy revealed that these nanoclusters were randomly oriented GaAs crystallites. An oxide outer shell of ~ 2 nm subsequently developed on the surfaces of the nanocrystals as a result of transportation of the cluster in air. Unpassivated GaAs nanoclusters exhibited no detectable photoluminescence. After surface passivation, these nanoclusters displayed photoluminescence energies less than that of the bulk GaAs from which they were made. These experiments suggest an abundance of sub-bandgap surface states in GaAs nanocrystals. Thus, this kind of nanocluster with a surface layer demonstrates that a decrease as well as an increase can be achieved with transition from the bulk to the nanoscale level. Such changes in the photoluminescence energy were similar to that observed with silicon clusters [83, 84].

7. PERSPECTIVES ON LASER ABLATION FOR CONTROLLABLE PRODUCTION OF NANOCLUSTERS

Laser ablation has proven to be an efficient and flexible tool for the production of a large variety of novel nanoclusters with remarkable properties. These novel nanostructures include fullerenes, carbon and boron nitride nanotubes, magnetic nanofoam, metal clusters, silicon clusters, and a variety of cluster-assembled films and nanofilms. It is clear that this is only the beginning; many different and complex clusters can be created and tested for future applications. Generation of nanoclusters by laser ablation is already a well-controlled process where the ablation rate, temperature and ionization states of the ablated atomic flux, and the conditions of the laser plume and ambient gas interaction can be controlled with high precision. Moreover, it is now clear that control over these processes in time and space can be significantly improved by the use of short laser pulses, as short as a few femtoseconds, and high repetition rate (up to hundreds of megaHertz) lasers. There are also some obvious extensions for the use of laser ablation for simultaneous coevaporation of several different targets for deposition of complex films or preparation of unusual composites and alloys. The same technique can be used for the preparation of multilayered systems consisting of nanometer-thick layers of different materials, which may be regarded as a one-dimensional analog of cluster-assembled films.

Nanoscience and nanotechnology are still in their infancy. However, one can easily foresee many short-term and long-term applications for nanoclusters and cluster-assembled structures.

The obvious short-term applications for cluster networks are in catalytic devices, systems with unusual and variable dielectric properties, and layers with controllable heat conduction. However, there will be also many long-term applications for nanoclusters, for example, as part of future nanodevices for nanoelectronics, nanophotonics, and spintronics. We may also mention nanowires of carbon nanotubes, nanometric metal-dielectric junctions, and ultra-low-capacitance devices comprising one or several nanoclusters, Coulomb-blockade structures where one-by-one passage of a single electric charge between two neighboring particles can be regulated.

The pulse duration, the intensity on the target surface, and the repetition rate can be precisely controlled in laser ablation, so precise and improved control over the ablated vapor can be achieved. Using lasers one can control heating and annealing rates on a space scale of micrometers and a time scale of femtoseconds. This improvement in the control of cluster formation conditions leads to realization of the atom-to-atom attachment mode of nanocluster building, increasing the possibilities for control over the cluster size and the internal structure of a cluster. Laser ablation is also a route for creating metastable allotropes of known materials where the unusual internal structure determines new material properties such as were seen in conducting carbon nanotubes or paramagnetic all-carbon nanofoam.

Laser ablation has demonstrated the highest deposition rate in the production of thin films, of $\sim 10 \mu\text{m/h}$ [73, 75], and of production of a nanofoam of $1 \text{ cm}^3/\text{min}$. If lasers can be made cost effective and manageable under industrial conditions, then the industrial production of nanostructures with the use of lasers is a distinct possibility in the near future.

Indeed, there is still a "plenty of room at the bottom" and lasers will help to fill it with new and amazing nanostructures.

GLOSSARY

ACKNOWLEDGMENT

The authors acknowledge Dr. D. Golberg for providing HRTEM photographs of single wall carbon nanotubes for the present review.

REFERENCES

1. Klaus Sattler, Ed., "Cluster Assembled Materials," Material Science Forum, Vol. 232. Trans Tech Publications Ltd., Switzerland 1996.
2. W. A. de Heer, The physics of simple metal clusters: Experimental aspects and simple models, *Rev. Mod. Phys.* 85, 611 (1993).
3. P. Milani and S. Iannotta, "Cluster Beam Synthesis of Nanostructured Materials." Springer-Verlag, Berlin, 1999.
4. A. H. Pfund, *Rev. Sci. Instrum.* 1, 397 (1930).
5. P. Marquardt, *Appl. Phys. A* 68, 211 (1999).

6. D. B. Chrisey and G. K. Hubler, Eds., "Pulsed Laser Deposition of Thin Films." Wiley, New York, 1994.
7. P. Caricato, G. Leggieri, A. Luches, A. Perrone, E. Gyorgy, I. N. Mihailescu, M. Popescu, G. Barucca, P. Mengucci, J. Zemek, and M. Trchova, *Thin Solid Films* 307, 54 (1997).
8. Rossi, B. Andre, A. van Ven, P. E. Mijnders, H. Schut, F. Labohm, M. P. Delplancke, H. Dunlop, and E. Anger, *Thin Solid Films* 253, 85 (1994).
9. C. Vivien, J. Hermann, A. Perrone, C. Boulmer-Leborgne, and A. Luches, *J. Phys. D: Appl. Phys.* 31, 1263 (1998).
10. Y. Nakata, H. Kaibara, T. Okada, and M. Maeda, *J. Appl. Phys.* 80, 2458 (1996).
11. H. F. Sakeek, T. Morrow, W. G. Graham, and D. G. Walmsley, *Appl. Phys. Lett.* 59, 3631 (1991).
12. T. J. Goodwin, V. J. Leppert, S. H. Risbud, I. M. Kennedy, and H. W. H. Lee, *Appl. Phys. Lett.* 70, 3122 (1997).
13. P. Verardi, M. Dinescu, F. Graciun, and A. Perrone, *Appl. Surf. Sci.* 127–129, 457 (1998).
14. S. Gill, A. A. Anderson, R. W. Eason, T. J. Warburton, and D. P. Shepherd, *Appl. Phys. Lett.* 69, 10 (1996).
15. S. Fukaya, T. Hasegawa, Y. Ishida, and M. Obara, High-power laser ablation, in "SPIE Proceedings, Advanced High-Power Lasers and Applications AHPLA'99," 3885-42, Osaka, Japan, 1–5 Nov., 1999.
16. V. E. Bondybey and J. H. English, *J. Chem. Phys.* 76, 2165 (1982).
17. S. J. Riley, E. K. Parks, C. R. Mac, L. G. Pobo, and S. Wexler, *J. Phys. Chem.* 86, 391 (1982).
18. Smalley, R. E., *Laser Chem.* 2, 167 (1983).
19. H. W. Kroto, J. R. Heath, S. C. O'Brien, R. F. Curl, and R. E. Smalley, *Nature* 318, 162 (1985).
20. S. Iijima, *Nature* 354, 56 (1991).
21. T. W. Ebbesen, Ed., "Carbon Nanotubes: Preparation and Properties." CRC Press, Boca Raton, 1996.
22. D. Golberg, Y. Bando, M. Eremets, K. Takemura, K. Kurashima, and H. Yusa, *Appl. Phys. Lett.* 69, 2045 (1996).
23. P. Calderola and H. Knoepfel, Eds., "Physics of High Energy Density," Proceedings of the International School of Physics "Enrico Fermi" Course XLVIII. Academic Press, New York, 1971.
24. S. I. Anisimov, Y. A. Imas, G. S. Romanov, and Y. V. Khodyko, "Action of High-Power Radiation on Metals." Consult. Bureau, Springfield, 1971.
25. J. F. Ready, "Effects of High Power Laser Radiation." Academic Press, New York, 1971.
26. R. L. McCrory, Laser-driven ICF experiments, Chap. 22 in "Nuclear Fusion by Inertial Confinement" (G. Velarde, Y. Ronen, and J. M. Martinez-Val, Eds.). CRC Press, Boca Raton, 1993.
27. T. Guo, P. Nikolaev, A. Thess, D. T. Colbert, and R. E. Smalley, *Chem. Phys. Lett.* 243, 49 (1995).
28. W. K. Maser, E. Muñoz, A. M. Benito, M. T. Martínez, G. F. de la Fuente, Y. Maniette, E. Anglaret, and J.-L. Sauvajol, *Chem. Phys. Lett.* 292, 587 (1998).
29. F. Kokai, K. Takahashi, M. Yudasaka, R. Yamada, T. Ichibashi, and S. Iijima, *J. Phys. Chem. B* 103, 4346 (1999).
30. M. Yudasaka, F. Kokai, K. Takahashi, R. Yamada, N. Sensui, T. Ichibashi, and S. Iijima, *J. Phys. Chem. B* 103, 3576 (1999).
31. E. G. Gamaly, A. V. Rode, and B. Luther-Davies, *J. Appl. Phys.* 85, 4213 (1999).
32. A. V. Rode, B. Luther-Davies, and E. G. Gamaly, *J. Appl. Phys.* 85, 4222 (1999).
33. M. D. Perry, B. C. Stuart, P. S. Banks, M. D. Feit, V. Yanovsky, and A. M. Rubenchik, *J. Appl. Phys.* 85, 6803 (1999).
34. A. V. Rode, A. Zakery, M. Samoc, E. G. Gamaly, and B. Luther-Davies, *Appl. Surf. Sci.* 197–198, 481 (2002).
35. A. V. Rode, M. Samoc, B. Luther-Davies, E. G. Gamaly, K. F. MacDonald, and N. I. Zheludev, *Optics Lett.* 26, 441 (2001).
36. E. G. Gamaly, A. V. Rode, O. Uteza, M. Samoc, and B. Luther-Davies, *Appl. Surf. Sci.* 197–198, 730 (2002).

37. A. V. Rode, S. T. Hyde, E. G. Gamaly, R. G. Elliman, D. R. McKenzie, and S. Bulcock, *Appl. Phys. A* 69 (Suppl.), S755 (1999).
38. V. Kolev, M. Lederer, B. Luther-Davies, A. Rode, H. Tan, and C. Jagadish, in "Proceedings of the Australian Institute of Physics 15th Biennial Congress 2002," Sydney, 8–11 July 2002.
39. A. V. Rode, E. G. Gamaly, and B. Luther-Davies, *Appl. Phys. A* 70, 135 (2000).
40. S. Arepalli, P. Nikolaev, W. Holmes, and C. D. Scott, *Appl. Phys. A* 70, 125 (2000).
41. W. Kautek, S. Pentzien, A. Conradi, J. Krüger, and K.-W. Brzezinka, *Appl. Surf. Sci.* 106, 158 (1996).
42. E. G. Gamaly, A. V. Rode, A. Perrone, and A. Zocco, Mechanisms of ablation rate decrease in multiple pulse laser ablation, *Appl. Phys. A* 73, 143 (2001).
43. A. A. Puzosky, H. Schittenhelm, Xudong Fan, M. J. Lance, L. R. Allard, Jr., and D. Geohegan, *Phys. Rev. B* 65, 245, 425 (2002).
44. E. G. Gamaly, A. V. Rode, and B. Luther-Davies, *Appl. Phys. A* 69(Suppl.), S121 (1999).
45. E. A. Rohlfing, D. M. Cox, and A. Kaldor, *J. Chem. Phys.* 81, 3322 (1984).
46. A. A. Puzosky, D. B. Geohegan, H. Schittenhelm, Xudong Fan, and M. A. Guillorn, *Appl. Surf. Sci.* 197–198, 552 (2002).
47. M. Born and E. Wolf, "Principles of Optics." Pergamon Press, Oxford, 1964.
48. E. G. Gamaly, A. V. Rode, W. K. Maser, E. Munoz, A. M. Benito, M. T. Martinez, and G. F. de la Fuente, *Appl. Phys. A* 70, 161 (2000).
49. M. Ge and K. Sattler, *Appl. Phys. Lett.* 65, 2284 (1994).
50. J. W. G. Wildoer, L. C. Venema, A. G. Rinzier, and R. E. Smalley, *Nature* 391, 59 (1998).
51. D. Golberg, Y. Bando, L. Bourgeois, and K. Kurashima, *Carbon* 37, 1858 (1999).
52. E. G. Gerstner, P. B. Lukins, D. R. McKenzie, and D. G. McCulloch, *Phys. Rev. B* 54, 14504 (1996).
53. J. Bulir, M. Jelinek, V. Vorlicek, D. Chvostova, and L. Soukup, *J. Non-Cryst. Solids* 188, 118 (1995).
54. A. V. Rode, E. G. Gamaly, and B. Luther-Davies, *Appl. Phys. A* 70, 135 (2000).
55. A. M. Rao, E. Richter, Shunji Bandow, Bruce Chase, P. C. Eklund, K. A. Williams, S. Fang, K. R. Subbaswamy, M. Menon, A. Thess, R. E. Smalley, G. Dresselhaus, and M. S. Dresselhaus, *Science* 275, 187 (1997).
56. M. S. Dresselhaus, G. Dresselhaus, and P. C. Eklund, "Science of Fullerenes and Carbon Nanotubes." Academic Press, New York, 1996.
57. R. F. Egerton, "Electron Energy-Loss Spectroscopy in the Electron Microscope." Plenum, New York, 1986.
58. S. D. Berger, D. R. McKenzie, and P. S. Martin, *Philos. Mag. Lett.* 57, 285 (1988).
59. S. Brunauer, P. H. Emmett, and E. Teller, *J. Phys. Chem.* 60, 309 (1938).
60. W. D. Harkins and G. Jura, *J. Chem. Phys.* 11, 431 (1942).
61. P. W. Schmidt, in "Modern Aspects of Small-Angle Scattering" (H. Brumberger, Ed.). Kluwer Academic, Dordrecht, 1995.
62. J. A. Leavitt, L. C. McIntyre, Jr., and M. R. Weller, Backscattering spectrometry, in "Handbook of Modern Ion Beam Material Analysis" (J. R. Tesmer and M. Nastasi, Eds.), pp. 37–81. MRS, Pittsburgh, 1995.
63. L. D. Landau and E. M. Lifshitz, "Electrodynamics of Continuous Media." Pergamon Press, Oxford, 1960.
64. W. L. Kruer, "The Physics of Laser Plasma Interaction." Addison-Wesley, New York, 1987.
65. E. G. Gamaly, A. V. Rode, and V. T. Tikhonchuk, *Phys. Plasmas* 9, 949 (2002).
66. Y. B. Zel'dovich and Y. P. Raizer, "Physics of Shock Waves and High-Temperature Hydrodynamic Phenomena." Academic Press, New York, 1967.
67. B. C. Stuart, M. D. Feit, S. Herman, A. M. Rubenchik, B. W. Shore, and M. D. Perry, *JOSA B* 13, 459 (1996).
68. P. P. Pronko, P. A. Van Rompay, C. Horvath, F. Loesel, T. Juhasz, X. Liu, and G. Mourou, *Phys. Rev. B* 58, 2387 (1998-I).
69. P. A. Van Rompay, M. Nantel, and P. P. Pronko, *Surf. Coatings Technol.* 100–101, 496 (1998).
70. D. Bauerle, "Laser Processing and Chemistry." Springer-Verlag, Berlin, 2000.
71. Experimental Methods in the Physical Sciences, Vol. 30, in "Laser Ablation and Desorption" (J. C. Miller and R. F. Haglund, Jr., Eds.). Academic Press, New York, 1998.
72. A. A. Voevodin and M. S. Donley, *Surf. Coatings Technol.* 82, 199 (1996).
73. E. G. Gamaly, A. V. Rode, and B. Luther-Davies, *Laser Particles Beams* 18, 245 (2000).
74. P. Pronko, P. A. Van Rompay, and S. Sato, "Proceedings of SPIE," Vol. 3269, 1998.
75. P. S. Banks, L. Donh, B. C. Stuart, M. D. Feit, A. M. Rubenchik, A. M. Komashko, M. D. Perry, and W. McLean, *Appl. Phys. A* 69, 347 (1999).
76. J. N. Leboeuf, K. R. Chen, J. M. Donato, D. B. Geohegan, C. L. Liu, A. A. Puzosky, and R. F. Wood, *Phys. Plasmas* 3, 2203 (1996).
77. M. P. Siegal, L. J. Martinez-Miranda, N. J. DiNardo, D. R. Tallant, J. C. Barbour, and P. M. Provencio, High Power Laser Ablation, "Proceedings of SPIE," Santa Fe, NM, 1998.
78. O. Eibl and B. Roas, *J. Mater. Res.* 5, 2620 (1990).
79. P. Schwab and D. Bauerle, *Physica C* 182, 103 (1991).
80. D. P. Norton and D. H. Lowndes, *Appl. Phys. Lett.* 63, 1432 (1993).
81. P. Gonzalez, R. Soto, E. G. Parada, X. Redondas, S. Chiussi, J. Serra, J. Pou, B. Leon, and M. Perez-Amor, *Appl. Surf. Sci.* 109–110, 380 (1997).
82. L. D. Landau and E. M. Lifshitz, "Statistical Physics." Pergamon Press, Oxford, 1980.
83. L. Patrone, D. Nelson, V. Safarov, M. Sentis, and W. Marine, *J. Luminescence* 80, 217 (1999).
84. W. Marine, L. Patrone, B. Luk'yanchuk, and M. Sentis, *Appl. Surf. Sci.* 154–155, 345 (2000).
85. M. Ge and K. Sattler, *Science* 260, 515 (1993).
86. E. G. Gamaly and L. T. Chadderton, *Proc. R. Soc. London Ser. A* 449, 381 (1995).
87. E. G. Gamaly, A. V. Rode, W. K. Maser, E. Munoz, A. M. Benito, M. T. Martinez, and G. F. de la Fuente, *Appl. Phys. A* 70, 161 (2000).
88. P. W. Anderson, "Basic Notions of Condensed Matter Physics." Benjamin/Cummings, Menlo Park, CA, 1984.
89. J. M. Kosterlitz and D. J. Thouless, *J. Phys. C: Solid State Phys.* 5, L124 (1972).
90. H. S. Seung and D. R. Nelson, *Phys. Rev. A* 38, 1005 (1988).
91. S. G. Kim and D. Tomanek, *Phys. Rev. Lett.* 72, 2418 (1994).
92. D. Tomanek, S. Mukherjee, and K. H. Benneman, *Phys. Rev. B* 28, 665 (1983).
93. S. J. Oh, S. H. Huh, H. K. Kim, J. W. Park, and G. H. Lee, *J. Chem. Phys.* 111, 7402 (1999).
94. S. H. Huh, H. K. Kim, J. W. Park, and G. H. Lee, *Phys. Rev. B* 62, 2937 (2000-II).
95. L. P. Gor'kov and G. M. Eliashberg, *Sov. Phys. JETP* 21, 940 (1965).
96. H.-P. Wu, A. Okano, and K. Takayanagi, *Appl. Phys. A* 71, 643 (2000).
97. M. V. Wolkin, J. Jorne, P. M. Fauchet, G. Allan, and C. Delerue, *Phys. Rev. Lett.* 82, 197 (1999).
98. T. Bachelis, R. Schafer, and H.-J. Guntherodt, *Phys. Rev. Lett.* 84, 4890 (2000).
99. E. Kaxiras and K. Jakson, *Phys. Rev. Lett.* 71, 727 (1993).
100. J. C. Grossman and L. Mitas, *Phys. Rev. B* 52, 16735 (1995).
101. J. Wang, X. Chen, G. Wang, B. Wang, Wei Lu, and J. Zhao, *Phys. Rev. B* 66, 085408 (2002).

102. Z. Liu, Y. Sakamoto, T. Ohsuma, K. Higara, O. Terasaki, C. H. Ko, H. J. Shin, and R. Ryoo, *Angew. Chem. Int. Ed. Engl.* 39, 3107 (2000).
103. K. B. Lee, S. M. Lee, and J. Cheon, *Adv. Mater.* 13, 517 (2001).
104. A. J. Dally and L. A. Bloomfield, *Phys. Rev. Lett.* 90, 063401 (2003).
105. J. P. Rose and R. S. Berry, *J. Chem. Phys.* 96, 517 (1992).
106. T. Jacob, S. Fritzsche, W.-D. Sepp, B. Fricke, and J. Anton, *Phys. Lett. A* 300, 71 (2002).
107. U. Krebig and M. Vollmer, "Optical Properties of Metal Clusters." Springer-Verlag, Berlin, 1995.
108. M. Brack, *Rev. Mod. Phys.* 65, 677 (1993).
109. R. Gao, Z. L. Wang, Z. Bai, W. A. de Heer, L. Dai, and M. Gao, *Phys. Rev. Lett.* 85, 622 (2000).
110. J. W. Mintmire, B. I. Dunlap, and C. T. White, *Phys. Rev. Lett.* 68, 631 (1992).
111. R. Saito, M. Fujita, G. Dresselhaus, and M. S. Dresselhaus, *Appl. Phys. Lett.* 60, 2204 (1992).
112. N. Hamada, S. Sawada, and A. Oshiyama, *Phys. Rev. Lett.* 68, 1579 (1992).
113. M. Schluter, M. Lannoo, M. Needels, G. A. Baraff, and D. Tománek, *Phys. Rev. Lett.* 68, 526 (1992).
114. A. V. Rode, E. G. Gamaly, A. G. Christy, S. T. Hyde, R. G. Elliman, B. Luther-Davies, A. I. Veinger, J. Giapintzakis, J. Androulakis, N. Park, M. Yoon, S. Berber, J. Ihm, E. Osawa, and D. Tománek, submitted for publication.
115. A. L. Mackay and H. Terrones, *Nature* 352, 762 (1991).
116. D. Vanderbilt and J. Tersoff, *Phys. Rev. Lett.* 68, 511 (1991).
117. S. T. Hyde, Crystalline frame works as hyperbolic films, in "Defects and Processes in the Solid State" (J. D. FitzGerald and J. N. Boland, Eds.). Elsevier, Amsterdam, 1993.
118. S. T. Hyde and M. O'Keeffe, *Philos. Trans. R. Soc. London Ser. A* 354, 1999 (1996).
119. S. Bandow, F. Kokai, K. Takahashi, M. Yudasaka, and S. Iijima, *Appl. Phys. A* 73, 281 (2001).
120. A. Krishnan, E. Dujardin, M. M. Treacy, J. Hugdahl, S. Lynam, and T. W. Ebbesen, *Nature* 388, 451 (1997).
121. J. Tersoff, *Phys. Rev. B* 46, 15546 (1992-I).
122. R. F. Curl, in "Buckminsterfullerenes" (E. W. Billups and M. A. Ciufolini, Eds.). VCH, New York, 1993.
123. P. W. Fowler and D. E. Manolopoulos, "An Atlas of Fullerenes." Clarendon Press, Oxford, 1995.
124. T. W. Ebbesen, *Phys. Today* 49, 26 (1996).
125. M. M. Treacy, T. W. Ebbesen, and J. M. Gibson, *Nature* 381, 678 (1996).
126. M. Gomberg, *J. Am. Chem. Soc.* 22, 757 (1900).
127. A. V. Zenkevich, M. A. Pushkin, V. N. Tronin, V. N. Nevolin, G. A. Maximov, D. O. Efimov, and E. Lagsgaard, *Phys. Rev. B* 65, 073406 (2002).
128. A. Perez, P. Melinon, V. Dupuis, P. Jensen, B. Prevel, J. Tuaillon, L. Bardotti, C. Martet, M. Treilleux, M. Broyer, M. Pellarin, J. L. Vaille, B. Palpant, and J. Lerme, *J. Phys. D: Appl. Phys.* 30, 709 (1997).
129. H. Haberland, Z. Insepov, and M. Moseler, *Phys. Rev. B* 51, 11061 (1995).
130. W. Harbich, S. Fedrigo, and J. Buttet, *Chem. Phys. Lett.* 195, 613 (1992).
131. W. Harbich, S. Fedrigo, J. Buttet, and D. M. Lindsay, *J. Chem. Phys.* 96, 8104 (1992).
132. Y. Qiang, R. F. Sabiryanov, S. S. Jaswal, Y. Liu, H. Haberland, and D. J. Sellmyer, *Phys. Rev. B* 66, 064404 (2002).
133. S. Vijayalakshmi, A. Lan, Z. Iqbal, and H. Grebel, *J. Appl. Phys.* 92, 2490 (2002).
134. G. Deutscher, A. M. Goldman, and H. Micklitz, *Phys. Rev. B* 31, 1679 (1985).
135. C. Roland, V. Meunier, B. Larade, and Hong Guo, *Phys. Rev. B* 66, 035332 (2002).
136. L. N. Dinh, S. E. Hayes, A. E. Wynne, M. A. Wall, C. K. Saw, B. C. Stuart, M. Balooch, A. K. Paravastu, and J. A. Reimer, *J. Mater. Sci.* 37, 3953 (2002).